Seismic Fragility Analysis based on Artificial Ground Motions and Surrogate Modeling of Validated Structural Simulators

G. Abbiati*[1], M. Broccardo[2], I. Abdallah[3], S. Marelli[3], and F. Paolacci[4]

[1]*Department of Engineering, Aarhus University, Denmark*
[2]*Department of Civil, Environmental and Mechanical Engineering, University of Trento, Italy*
[3]*Department of Civil, Environmental and Geomatic Engineering, ETH Zurich, Switzerland*
[4]*Department of Engineering, Roma Tre University, Italy*

Draft submitted to *engrXiv*

October 12, 2020

Abstract

This study introduces a computational framework for efficient and accurate seismic fragility analysis based on a combination of artificial ground motion modeling, polynomial-chaos-based global sensitivity analysis, and hierarchical kriging surrogate modeling. The framework follows the philosophy of the Performance-Based Earthquake Engineering PEER approach, where the fragility analysis is decoupled from hazard analysis. This study addresses three criticalities that are present in the current practice. Namely, reduced size of hazard-consistent size-specific ensembles of seismic records, validation of structural simulators against large-scale experiments, high computational cost for accurate fragility estimates. The effectiveness of the proposed framework is demonstrated for the Rio Torto Bridge, recently tested using hybrid simulation within the RETRO project.

1 Introduction

The PEER Performance-Based Earthquake Engineering (PBEE) framework is widely used to perform seismic risk analysis. The framework is a simple statement of the total probability theorem, which combines the output of Probabilistic Seismic Hazard Analysis (PSHA) with fragility, damage, and loss analysis. A critical part of the framework is the coupling between hazard and structural modeling, namely, fragility analysis. It comes as no surprise that it developed into a stand-alone research field. Given a structural system of interest, the most recent advancement in fragility analysis requires the selection of a set of suitable ground motions to be used as input for non-linear structural analysis. Then, the statistics of a Quantity of Interest (QoI), which in general is denoted as Engineering Demand Parameter (EDP), are derived as a function of a given Intensity Measure (IM), or a vector of IMs. Specifically, these conditional EDP-IM relations are named fragility functions. Following this line, in recent years, a lot of research has been devoted to creating computational fragility frameworks, including the selection and the use of real seismic records and non-linear time history analysis. An incomplete list of studies in this topic includes [1, 2, 3, 4]. However, within this perimeter, a number of open issues have been raised by the opinion paper of Bradley [5] and further elaborated in the state-of-the-art review of Silva and co-authors [6]. Departing from these studies, this paper aims to address three criticalities:

1. In recent years, there have been significant advancements in ground motion selection procedures, which have partially solved the problem of defining a suitable set of seismic records for structural analysis. However, although these selections are sufficient to describe important characteristics of the hazard for a given structure of interest, the number of available records is usually insufficient to compute accurate estimates of the QoIs statistics.

*Corresponding Author: Dr. Giuseppe Abbiati, `abbiati@eng.au.dk`, ORCID: `0000-0002-5048-8505`.

2. The validation of structural simulators and the quantification of the associated model uncertainty against representative experiments—despite being critical—is often overlooked. This is due to practical reasons. Structural testing is usually not affordable beyond the component level due to the limited capacity of experimental facilities. Also, the budget allocated for structural testing is typically sufficient for running a small number of destructive experimental tests, which cannot cover the entire range of IMs for the fragility analysis.

3. The computation of fragility analysis requires a large number of time history analyses. It follows that computational cost of structural simulators limit *de facto* the total number of simulations. This is a classical problem in simulation-based Uncertainty Quantification (UQ), which is tackled by replacing the computationally expensive simulator with an equivalent (with respect to, w.r.t., the QoI) response surface a.k.a. surrogate model. However, defining surrogate models for non-linear dynamic analysis is challenging and still not completely addressed by the current state of the art of fragility computation. As a consequence, the accuracy of the fragility is limited by available computational resources.

This study introduces a computational framework for efficient and accurate seismic fragility analysis based on a combination of artificial ground motion modeling and surrogate modeling. Moreover, the goal is to integrate the know-how developed in ground motion selection and to follow the original spirit of the PEER-PBEE framework to decouple the task of hazard and fragility analysis. Specifically, given a suitable set of real seismic time series, we define an artificial ground motion model equipped with engineering-meaningful parameters. The selected real seismic time series are thought of as realizations of the ground motion model, using the same philosophy introduced by [7, 8]. Unlike their work, this framework uses the real seismic time series to calibrate the parameters of the artificial ground motion model and the associated uncertainties. The definition of such a hazard model poses the basis for using a surrogate-based UQ forward analysis.

The building blocks of the computational framework are: the artificial ground motion model, an expensive-to-evaluate High-Fidelity (HF) structural simulator of the reference structure *validated* against experiments (e.g., Hybrid Simulation (HS) in the proposed application [9]), and a corresponding cheaper Low-Fidelity (LF) structural simulator (e.g., obtained via dynamic substructuring of the HF simulator in this study [10]). The seismic vulnerability analysis follows these sequential steps: i) generation a family of artificial motions (compatible with the real selected ones); ii) computation of the Polynomial Chaos Expansion (PCE) of the LF simulator QoI prediction; iii) dimensionality reduction of the artificial ground motion parameters based on Global Sensitivity Analysis (GSA); iv) computation of a Hierarchical Kriging (HK) surrogate that fuses LF and HF predictions of the QoI; v) the fragility analysis is derived as a natural byproduct of the framework.

Fragility analysis and, more broadly, seismic risk assessment based on stochastic simulations is not new, and an incomplete list of studies includes [11, 12, 13, 14]. Moreover, to the best of our knowledge, the first study using also kriging surrogate modeling is [15] and more recently [16]. Different form the previous contributions, this paper draws a direct link between ground motion selection and the calibration of the stochastic hazard model; moreover, it introduces HK to combine predictions of simulators with different degrees of fidelity. In essence, the artificial ground motion model is used to build a large ensemble of time series, which would not be possible to compose using records of real seismic events. Therefore, this study aims to bridge classical seismic fragility analysis with the most recent UQ advancements, and not to solve the full seismic risk analysis (as done in [15] by fully employing the philosophy of [8]). In this context, this paper introduces a combination of PCE-based GSA and HK so that the computational burden associated with the fragility analysis is drastically reduced.

The framework is applied to a real-world application consisting of a Reinforced Concrete (RC) bridge case study, which was recently tested within the RETRO project [17, 18]. LF and HF simulators are introduced, highlighting the crucial role of HS in enabling experimental validation of the bridge model [19]. Since the selected case study structure is insensitive to broadband ground motions, the artificial ground motion model incorporates a pulse-like component [20], and it is calibrated against a set hazard-consistent site-specific real records. The framework is applied to compute the fragility analysis related to the lateral drift of one of the twelve piers of the Rio Torto Bridge.

This paper is organized as follows. Section 2 describes the proposed seismic fragility analysis framework. Section 3 introduces the Rio Torto Bridge case study. Section 4 describes both HF and LF structural simulators of the bridge. Section 5 describes the calibration of the artificial ground motion model using hazard-compatible site-specific seismic records. Section 6 summarizes the results of the seismic fragility analysis of the bridge. Section 7 includes limitations, future perspectives, and conclusions. For the sake of completeness, the entire machinery of surrogate modeling and, in particular, PCE-based GSA [21, 22] and HK [23] are reported as appendices providing a self-consistent notation.

2 Seismic fragility analysis framework

2.1 Theoretical background

Let $A(t)$ denote the stochastic process representing the input excitation of the system. The goal is to represent the process in terms of an aleatory component (i.e., the inherent variability of the process) and an epistemic component (i.e., the parametric variability of the process). Accordingly, it is convenient to express $A(t)$ as follows.

$$A(t) = \mathcal{M}_a(t, \boldsymbol{Z}|\boldsymbol{X}_a), \tag{1}$$

where $\mathcal{M}_a$ is a parametric stochastic model (or synthesis formula), $\boldsymbol{Z}$ is a set of random variables representing the aleatory variability, and $\boldsymbol{X}_a$ a is a set of model parameters. In this setting, the model parameters are considered as random variables. However, this uncertainty is epistemic (i.e., can be reduced). Let Y denote the response QoI of a real system (e.g., the maximum displacement or internal force of a structural component), and $\mathcal{M}_c(A(t)|\boldsymbol{X}_c)$ a suitable (w.r.t. the QoI) structural simulator, where $\boldsymbol{X}_c$ is a set of model parameters. It follows that Y, can be written as

$$\begin{aligned} Y &= \mathcal{M}_c\left(\mathcal{M}_a(t, \boldsymbol{Z}|\boldsymbol{X}_a)|\boldsymbol{X}_c\right), & (2)\\ &= \mathcal{M}_s\left(\boldsymbol{Z}|\boldsymbol{X}\right), & (3)\end{aligned}$$

where $\mathcal{M}_s := \mathcal{M}_c \circ \mathcal{M}_a$ and $\boldsymbol{X} = [\boldsymbol{X}_a; \boldsymbol{X}_c]$. Observe that while $\mathcal{M}_c$ is a deterministic structural simulator, $\mathcal{M}_s$ is a stochastic simulator. In fact, given a realization of the model parameters, $\boldsymbol{x}$, Y is still a random variable with aleatory uncertainty determined by the propagation of $\boldsymbol{Z}|\boldsymbol{x}$. Using Eq.3, the Cumulative Distribution Function (CDF) of Y, denoted by $F_Y(y)$, can be written as

$$F_Y(y) = \mathbb{P}(\mathcal{M}_s(\boldsymbol{Z}|\boldsymbol{X}) \leq y) = \int_{\boldsymbol{x}}\int_{\boldsymbol{z}} \mathbb{I}\left(\mathcal{M}_s(\boldsymbol{z}|\boldsymbol{x}) \leq y\right) dF_{\boldsymbol{Z}}(\boldsymbol{z}) dF_{\boldsymbol{X}}(\boldsymbol{x}), \tag{4}$$

where $\mathbb{I}(\cdot)$ denotes the indicator function, $\mathbb{P}(\cdot)$ denotes probability, $F_{\boldsymbol{Z}}(\boldsymbol{z})$, $F_{\boldsymbol{X}}(\boldsymbol{x})$ denote the joint CDFs, and $dF_{\boldsymbol{Z}}(\boldsymbol{z}) = f_{\boldsymbol{Z}}(\boldsymbol{z})d\boldsymbol{z}$, $dF_{\boldsymbol{X}}(\boldsymbol{x}) = f_{\boldsymbol{X}}(\boldsymbol{x})d\boldsymbol{x}$, with $f_{\boldsymbol{X}}(\boldsymbol{x})$ and $f_{\boldsymbol{Z}}(\boldsymbol{z})$ being the joint probability densities. Observe that $\boldsymbol{Z}$ is statistically independent of $\boldsymbol{X}$; moreover, $f_{\boldsymbol{X}}(\boldsymbol{x}) = f_{\boldsymbol{X}_c}(\boldsymbol{x}_c) f_{\boldsymbol{X}_a}(\boldsymbol{x}_a)$ under the (reasonable) assumption that the parameters of the seismic input and the structural simulator are statistically independent. Next, the conditional CDF of Y given a realization $\boldsymbol{x}$ is simply

$$F_{Y|\boldsymbol{X}}(y|\boldsymbol{x}) = \mathbb{P}(\mathcal{M}_s(\boldsymbol{Z}|\boldsymbol{X} = \boldsymbol{x}) \leq y) = \int_{\boldsymbol{z}} \mathbb{I}\left(\mathcal{M}_s(\boldsymbol{z}|\boldsymbol{x}) \leq y\right) dF_{\boldsymbol{Z}}(\boldsymbol{z}). \tag{5}$$

Given the distribution function $F_{Y|X}$, the p-quantile function returns the value y_p such that $F_{Y|\boldsymbol{X}}(y_p|\boldsymbol{x}) = p$. Assuming $F_{Y|\boldsymbol{X}}$ is continuous and strictly monotonically increasing, $y_p = F^{-1}_{Y|\boldsymbol{X}}(p|\boldsymbol{x})$. However, since $\boldsymbol{X}$ is a random variable, y_p is also a random variable and can be written as

$$Y_p = F^{-1}_{Y|\boldsymbol{X}}(p|\boldsymbol{X}) = \mathcal{M}_p(\boldsymbol{X}). \tag{6}$$

where, for convenience, we define $\mathcal{M}_p(\cdot) := F^{-1}_{Y|\boldsymbol{X}}(p|\cdot)$, and $p \in [0, 1]$. Therefore, Y_p can also be viewed as stochastic process indexed by p. Moreover, $\mathcal{M}_p$ is a deterministic model, since the aleatory variability has been marginalized in Eq.6.

Given this general framework, a few observations need to be done for this specific study. First of all, $A(t)$ is artificial ground motion model, and $\boldsymbol{X}_a$ is a physically meaningful set of ground motions parameters. Specifically, the model is a Gaussian filtered white noise, therefore, $\boldsymbol{Z}$ is a set of standard normal random variables (more details in Section 5). Second, $\mathcal{M}_c$ is a structural simulator, and $\boldsymbol{X}_c$ is the set of model parameters. Finally, observe that despite its simplicity, Eq.6 involves a complex and highly non-trivial computational endeavor. In the following, this task is tackled using a non-intrusive UQ approach that assumes that $\mathcal{M}_c$ (and therefore $\mathcal{M}_s$) is a black-box solver.

2.2 Computational solution

In the context of earthquake engineering, the goal of this study is to determine the distribution of Y_p for different values of p. In general, the analytical solution of Eq.6 is not available; moreover, a classical Monte-Carlo-based solution is computationally prohibitive. In fact, $\mathcal{M}_c$ is an "expensive" model and, therefore, also $\mathcal{M}_p$. A natural alternative to drastically reduce the computational cost is to replace the original model with a surrogate model. Let $\hat{\mathcal{M}}_p$ denotes a surrogate model of $\mathcal{M}_p$, then

$$\hat{Y}_p = \hat{\mathcal{M}}_p(\boldsymbol{X}), \tag{7}$$

where $\hat{Y}_p \approx Y_p$. The statistics of $\hat{Y}_p$ are then directly used for decision making. The surrogate model should be compatible with the artificial ground motion model, an HF *validated* structural simulator and the chosen QoI. Specifically, the proposed scheme builds on a combination of PCE-based GSA and HK, and it is here summarized in the following steps.

1. **Model definition and validation.** Define the QoI, a stochastic model of the input $\mathcal{M}_a$ (Section 5), and a set of structural simulators $\mathcal{M}_c$ (Section 4). In this study, $c \in \{LF, HF\}$ where $c = HF$ corresponds to the expensive-to-evaluate HF simulator whereas $c = LF$ to a computationally cheaper LF simulator (Section 2.2 provides further detail on this choices). The definition of the models reflects the following criteria:

   (a) The artificial ground motion model is defined w.r.t. a local seismic catalog based on an *existing* suitable ground motion selection (e.g., [24, 25, 26]). In fact, this framework is designed to work complementary to any ground motion selection criteria, rather than to express a preference for specific selection criterion or to propose a new one.

   (b) The HF simulator successfully passed a comprehensive *validation* protocol. Validation entails a comparison of model predictions with physical experiments that adequately reproduce the real structural behavior [27]. This study uses HF simulators validated using HS. This minimizes the cost of conducting realistic structural testing campaigns compared to shake table testing [9]. To be robust to generalization error, the HF simulator incorporates an accurate description of the physics of the real structure, which includes geometric and material properties. Therefore, it is ranked first in terms of computational cost for a single evaluation amongst all structural simulators $\mathcal{M}_c$. As a result, the HF simulator is expected to succeed in representing the structural response with predetermined accuracy within a given validation domain.

   (c) The LF simulator is a computationally cheaper proxy of its HF counterpart. In principle, there are no constraints on the types of allowed model simplifications. For example, one could decide using different modeling paradigms for HF and LF simulators or 2D versus 3D geometrical representations. However, the mathematical assumption underlying HK surrogate modeling is that the bias of the LF simulator has a lower frequency content compared to the response of the HF simulator. Hence, this study proposes to derive the LF simulator as a reduced-order representation of the HF simulator using dynamic substructuring [10]. In particular, it is shown how to obtain a non-linear reduced-order model as an assembly of reduced-order linear components [28] connected by non-linear springs.

2. **Global-sensitivity-based dimensionality reduction.** Create a large Experimental Design (ED) $\{\boldsymbol{\mathcal{Y}}_{LF,p}, \boldsymbol{\mathcal{X}}\}$, where $\boldsymbol{\mathcal{Y}}_{LF,p} = \{y_{LF,p}^{(1)}, \ldots, y_{LF,p}^{(N_{LF})}\}$, $\boldsymbol{\mathcal{X}} = \{\boldsymbol{x}^{(1)}, \ldots, \boldsymbol{x}^{(N_{LF})}\}$, $\boldsymbol{x}^{(n)}$ is a generic sample of the input parameters, and $y_{LF,p}^{(n)}$ is the corresponding LF estimate of the p-quantile of the QoI. Train a non intrusive PCE surrogate model [21], $\hat{\mathcal{M}}_{LF,p}^{PCE}(\boldsymbol{x})$, based on $\{\boldsymbol{\mathcal{Y}}_{LF,p}, \boldsymbol{\mathcal{X}}\}$. Perform a PCE-based GSA [22] w.r.t. the QoI. Select and retain the input random variables that contribute most to the variability (variance) of the QoI and fix the remaining ones to their expected value. In practice, define $\boldsymbol{X} = [\boldsymbol{X}_\alpha, \boldsymbol{x}_\beta]$, where $\boldsymbol{X}_\alpha$ are the "important random variables," and $\boldsymbol{x}_\beta = E[\boldsymbol{X}_\beta]$ the rest of input parameters. A natural output of GSA are univariate effects of input parameters, which are the expectation of a QoI conditioned to the value of a single input variable (therefore, they provide information about the shape of the surrogate models). In this context they are used at step 4 for defining monotonic fragility models. A detailed summary on PCE-based GSA is reported in Appendix A.

3. **Hierarchical Kriging surrogate modeling.** Train a second smaller ED $\{\boldsymbol{\mathcal{Y}}_{HF,p}, \boldsymbol{\mathcal{X}}_\alpha\}$, where $\boldsymbol{\mathcal{Y}}_{HF,p} = \{y_{HF,p}^{(1)}, \ldots, y_{HF,p}^{(N_{HF})}\}$, $\boldsymbol{\mathcal{X}}_\alpha = \{\boldsymbol{x}_\alpha^{(1)}, \ldots, \boldsymbol{x}_\alpha^{(N_{HF})}\}$, $\boldsymbol{x}_\alpha^{(n)}$ is a generic sample of the selected model parameters, and $y_{HF,p}^{(n)}$ is the corresponding HF estimate of the p-quantile of the QoI. Train a HK surrogate $\hat{\mathcal{M}}_{HF,p}^{K}(\boldsymbol{x}_\alpha)$ based on $\{\boldsymbol{\mathcal{Y}}_{HF,p}, \boldsymbol{\mathcal{X}}_\alpha\}$ using the PCE surrogate model of the LF structural simulator as trend function [29, 23]. A short summary of HK surrogate modeling is reported in Appendix B.

4. **Probabilistic characterization of the QoI.** Compute the statistics of the QoI of interest (including fragility analysis) via Monte-Carlo-based UQ analysis using the HK surrogate model. Specifically, given an ordered sequence of quantiles $\mathcal{P} = [p_1, ..., p_n]$, steps 2-3 can be implemented sequentially to obtain n maps (i.e., surrogate models) between $\boldsymbol{Y}_{\mathcal{P}}$ and $\boldsymbol{X}$. Therefore, this n ordered sequence of surrogate models provides the complete discretized CDF of the QoI w.r.t. the input $\boldsymbol{X} = \boldsymbol{x}$, i.e. $F(y_{\mathcal{P}}|\boldsymbol{x})$. Observe that such description is sufficient for a fast inversion of Eq.6. Finally, fragility models of the QoI w.r.t. the important random variables ($\boldsymbol{X}_\alpha$) are computed by MCS. Observe, that not all the *marginal* fragility w.r.t. the single important variables are necessarily monotonous. Therefore, following the current practice, only the monotonic increasing fragility are suitable for the PEER-PBEE framework. The univariate effects of QoI quantiles computed at step 2 guides this final selection.

Despite the use of stochastic simulators (Eq.3), the outlined framework has the critical advantage of providing by construction (Eq.6) a—deterministic—map between the input parameters and a given quantile of the distribution of the QoI. The nature of the uncertainty associated with this distribution is aleatory. Specifically, it is the aleatory component, $\boldsymbol{Z}$, of the stochastic model, $\mathcal{M}_s(\boldsymbol{Z}|\boldsymbol{x})$. In fact, in the special case of a deterministic simulator any quantile will collapse into the deterministic solution of $\mathcal{M}_c(\boldsymbol{x})$. A cornerstone of the proposed framework is model calibration and validation with experimental data. In fact, the LF simulator $\mathcal{M}_{LF}$ can be characterized by an oversimplification of the real problem, phenomenological (and not validated) assumptions, and non-physical parameters. As a result, a rigorous global model validation becomes prohibitive, leading to not negligible model biases. On the other hand, the advantage of LF structural simulators lies in their reduced computational cost, enabling global studies. Few considerations need to be made in the context of earthquake engineering. In this case, an EDP of interest is the QoI; moreover, a vector of $\boldsymbol{IM}$s is composed by either some of the "important" input parameters (i.e., $\boldsymbol{IM} \in \boldsymbol{X}_\alpha$) or by a set of instrumental IMs ($\boldsymbol{IM} = [PGA, PGV, ...]$). In the latter case, a statistical conversion [30] between the ground motion parameters and the instrumental IMs can be easily derived provided a large set of simulations. The proposed framework allows the computation of any statistic of interest for the selected EDP, including classical fragility functions and surfaces. In the fragility analysis context, a key passage of this framework is the GSA (step 2), which provides a rigorous selection of the important input parameters (i.e., $\boldsymbol{IM}$) w.r.t. to the EDP variability. Observe, that this condition is explicitly dependent on the quantile of (major) interest. Therefore, it potentially eliminates the loss of correlation between $\boldsymbol{IM}$ and EDP in the tail of fragility functions [31] (if this probability region is of interest).

3 The Rio Torto Bridge case study

The Rio Torto Bridge is a RC structure built in the '70s and located on the motorway between Florence and Bologna, Italy. The bridge comprises two independent roadways, each of 400 m length and characterized by a 13-span deck sustained by twelve piers. Three out of thirteen spans accommodate Gerber saddles, which protect the deck from restrained deformation due to pier settlement. Pier heights vary between a minimum of 13.80 m (Pier # 12) to a maximum of 41.00 m (Pier # 7). Figure 1a provides an overview of Rio Torto Bridge. The Rio Torto Bridge was selected as a case study to investigate the seismic performance of old RC bridges and possible seismic retrofitting schemes within the framework of the RETRO project [17]. The seismic response of the bridge was evaluated via HS. In detail, mock-up models of Pier #9 and #11 of 1:2.5 scale were built and tested via HS at ELSA Laboratory of the Joint Research Centre of Ispra, Italy. Figure 1b reports a schematic of the hybrid model of the Rio Torto Bridge. Non-linear springs represent the in-plane stiffness of numerical and physical piers activated by the lateral displacement of the deck. A schematic view of tested piers is also reported in Figure 1b. Figure 2a reports a schematic of the experimental setup conceived for Pier #11. In this specific case, actuators labeled 1A and 3B control the lateral in-plane displacement of the pier whereas, hydraulic jacks labeled 1B and 2B impose vertical forces owing to the deck weight. Figure 2b provides a picture of the entire installation at the JRC of Ispra. The East-West and the North-South components of the Emilia earthquake of May 29, 2012, recorded from Mirandola station and downloaded from the ITACA database [32] were considered as serviceability and ultimate limit state accelerograms (SLS and ULS, respectively). The response spectra of both SLS and ULS accelerograms are shown in Section 5 where the stochastic modeling of the seismic input for the fragility analysis is described. In this study, the uncertainty on the structural simulator parameters is considered negligible w.r.t. the ground motion parameters, therefore, we set $\boldsymbol{X}_c = \bar{\boldsymbol{x}}_c{}^*$, and $\boldsymbol{X} \equiv \boldsymbol{X}_a$. For a comprehensive description of the HS campaign, the reader is addressed to [18].

*This corresponds to assign a delta Probability Density Function, i.e., $\delta(\boldsymbol{x}_c - \bar{\boldsymbol{x}}_c)$

(a)

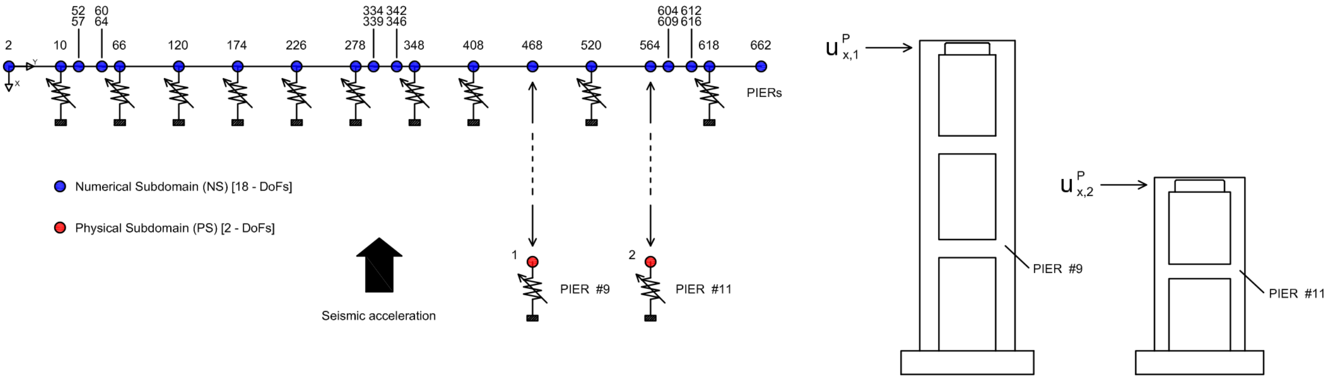

(b)

Figure 1: The Rio Torto Bridge case study: a) side view retrieved from [18]; b) hybrid model.

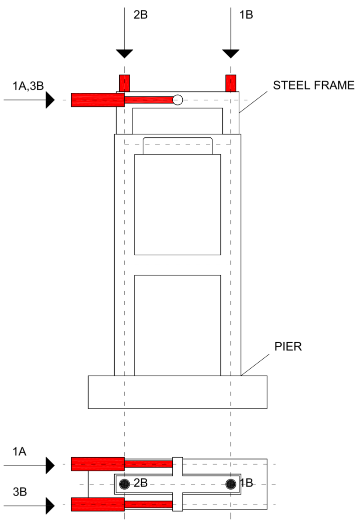

(a)

(b)

Figure 2: HS setup at JRC ispra: a) frontal and top view of Pier #11 retrieved from [19]; b) picture of the setup from top retrieved from [18].

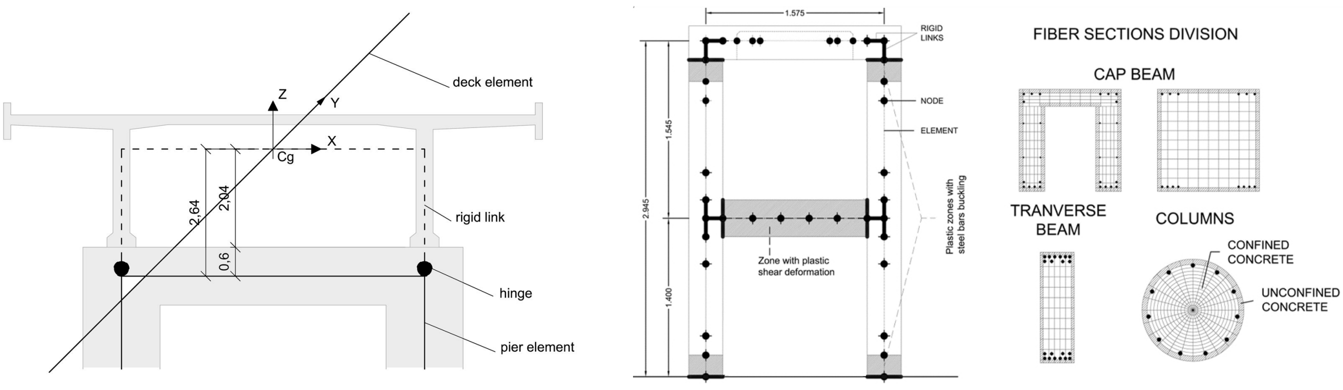

(a) (b)

Figure 3: HF simulator of the Rio Torto Bridge: a) deck-to-pier connection b) pier discretization and fibre-based cross-sections.

4 Computational modeling of the bridge

Two structural simulators of a single lane of the Rio Torto Bridge were implemented, namely, a HF finite-element and a LF state-space structural simulator. The former was initially implemented in OpenSees [33] to support the design of the experimental campaign. The latter was obtained, instead, via dynamic substructuring of the HF simulator to assemble reduced-order numerical substructures for HS [18]. Accordingly, LF and HF structural simulators show almost the same response in the linear regime.

4.1 High-fidelity finite-element model

The HF simulator was implemented in OpenSees [33]. Linear Bernoulli beam elements were used for the deck, whose response was assumed not to exceed the linear regime. Cylindrical hinges model Gerber saddles allowing for lateral and vertical rotations between deck elements while blocking relative torsional rotations. Displacement Degrees-of-Freedom (DoFs) of both abutments were constrained, but not rotations. A rigid link accounted for the offset distance between the cap beam axis, and the center of gravity of the deck cross-section. Each pier was clamped at the base. Figure 3 provides schematic views of both deck cross-section and finite-element discretization of piers.

All piers were modeled using non-linear fiber-based elements that allow for discretizing the longitudinal steel reinforcement of the member cross-section. The zero-tensile-strength *Concrete01* OpenSees material was adopted for concrete assuming a compressive strength $f_{pc} = -11.47$ MPa and $_{pc} = -17.16$ MPa for piers characterized by solid and hollow cross-section columns, respectively. These values were calibrated based on the quasi-static response of Pier #9 and #11 obtained via HS. In both cases, the ultimate concrete compressive strength was computed as $f_{pc,u} = 0.88 f_{pc}$ MPa and the Poisson ratio was set to $\nu = 0.2$. Corresponding strain values were set to $\epsilon_{pc} = -0.002$ and $\epsilon_{pc,u} = -0.006$, respectively. The *Steel02* OpenSees material was adopted for steel rebars assuming a tensile strength $f_y = 360$ MPa, along with a Young modulus $E = 205 \times 10^3$ MPa and hardening modulus $E_p = 0.025E$. The *Pinching4* OpenSees material was used to model the hysteretic shear response of transverse beam elements. Parameter values were calibrated for a series of cyclic tests conducted on a 1/4 scale mock-up model of Pier #12 documented in [34]. The OpenSees *section-aggregator* object was used to couple bending and shear models within the same force-based beam element. Finally, a proportional Rayleigh damping model was adopted with mass multiplier $\alpha_d = 0.27300$ and stiffness multiplier $\beta_d = 0.00787$. Figure 4 compares the hysteretic loop of the lateral restoring force of Pier #11 obtained via HS (SLS and ULS accelerograms, *as built* configuration) to corresponding HF simulator predictions. As can be appreciated, the HF simulator effectively reproduces the lateral restoring force response of Pier #11. A single evaluation of the time history response of the HF simulator subjected to a 15 sec accelerogram sampled at 1 msec takes about 10 min if performed with a standard laptop equipped with an Intel 1.80 GHz i7-8565U CPU and 16 GB RAM or similar.

4.2 Low-fidelity state-space model

A linearized version of the HF simulator supported the computation of reduced-order mass and stiffness matrices of deck and piers of the LF simulator via component-mode synthesis [28], which is a specific dynamic

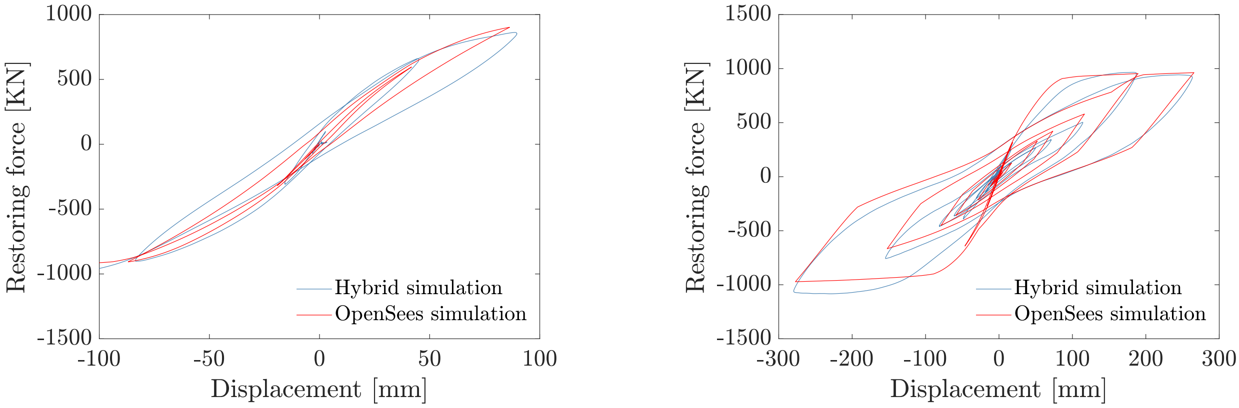

(a) (b)

Figure 4: Measured and simulated hysteresis loops of the lateral restoring force of Pier #11: a) SLS; b) ULS.

substructuring method [10]. In detail, the reduced-order model of the deck was obtained via static condensation retaining only lateral displacement DoFs of piers and Gerber saddles,

$$\begin{cases} \dot{\boldsymbol{u}} = \boldsymbol{v} \\ \dot{\boldsymbol{v}} = \boldsymbol{m}^{-1} \left(\boldsymbol{l} \cdot \boldsymbol{r} - \boldsymbol{c} \cdot \boldsymbol{v} - \boldsymbol{k} \cdot \boldsymbol{u} - \boldsymbol{t} \cdot a_g(t) \right), \end{cases} \tag{8}$$

where $\boldsymbol{u}$ and $\boldsymbol{v}$ are the 18 retained displacement and velocity DoFs, respectively; $\boldsymbol{k}$, $\boldsymbol{c}$ and $\boldsymbol{m}$ are reduced-order stiffness, damping and mass matrices, respectively, whereas $\boldsymbol{t}$ is the seismic mass vector. The latter multiplies the seismic accelerogram $a_g(t)$ to obtain the seismic loading. The 18×12 Boolean matrix $\boldsymbol{l}$ collocates the 12 pier restoring forces stored in $\boldsymbol{r} = \{r_1, \ldots, r_{12}\}$ to the related state-space equation. A non-linear single-DoF system based on a Bouc-Wen restoring force was calibrated to mimic the response of the corresponding pier in the HS structural simulator,

$$\begin{cases} \dot{u}_i = v_i \\ \dot{v}_i = m_i^{-1} \left[g_i(t) - c_i v_i - r_i - t_i a_g(t) \right] \\ \dot{r}_i = \left[A_i + \left(\beta_i \operatorname{sign}(r_i v_i) - \gamma_i \right) |r_i|^n \right] v_i, \end{cases} \tag{9}$$

where u_i, v_i, and r_i are the three state variables, namely, displacement, velocity, and hysteretic restoring force, whereas $g_i(t)$ represent the deck reaction force of the i-th pier. Mass m_i and seismic mass t_i were obtained via static condensation as well. For each pier, the top lateral displacement DoF was retained as master DoF, whereas the others were condensed. Consistently with the HF simulator, viscous damping c_i was computed assuming a proportional Rayleigh damping with mass multiplier $\alpha_d = 0.27300$ and stiffness multiplier $\beta_d = 0.00787$. The parameters A, β, γ and n refer to the Bouc-Wen model [35], which describes the evolution of the hysteretic restoring force r_i. As analogously done for damping, mass, and seismic mass, the parameter A, which represents the initial stiffness of the non-linear spring, was obtained via static condensation of the HF pier model. On the other hand, n was assumed constant and equal to one, whereas β and γ were calibrated to match the static response of the corresponding OpenSees pier model subjected to ten sinusoidal displacement cycles producing 0.5 % drift. Regarding Pier #11, Figure 5 compares restoring force, dissipated energy history and hysteresis loop of the calibrated Bouc-Wen spring to the corresponding OpenSees simulation. As can be appreciated from the figure, the Bouc-Wen spring fairly reproduces both restoring force peak and dissipated energy of the corresponding OpenSees model. Figure 6 compares the dynamic response of Pier #11 obtained from time history analyses of LF and HF structural simulators considering the ULS accelerogram of the HS campaign described in Section 3. A single evaluation of the time history response of the LF simulator subjected to a 15 sec accelerogram sampled at 1 msec performed with a standard laptop equipped with an Intel 1.80 GHz i7-8565U CPU and 16 GB RAM takes about 20 sec.

5 Stochastic modeling of the seismic input

The lateral motion of the Rio Torto Bridge is characterized by a relatively long period of vibration. Consequently, its reliability is not strongly affected by classic broadband motions. On the contrary, it is vulnerable to pulse like motions with frequencies close to the structural ones. Generally, the presence of a strong pulse component is more likely in near field motions. As a consequence, this study employs the stochastic model proposed by Dabaghi and Der Kiureghian [20], which is designed for such type of excitations.

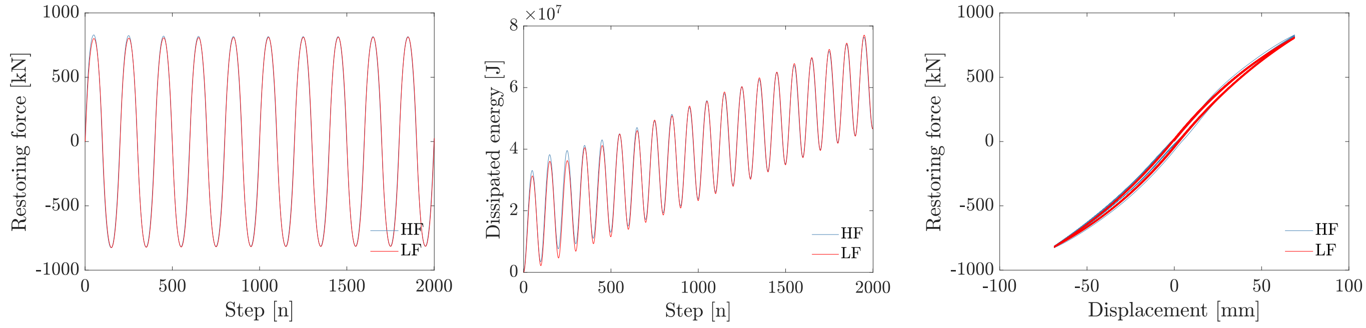

(a) (b) (c)

Figure 5: LF and HF predictions of the cyclic response of Pier #11: a) restoring force, b) dissipated energy, c) hysteresis loop.

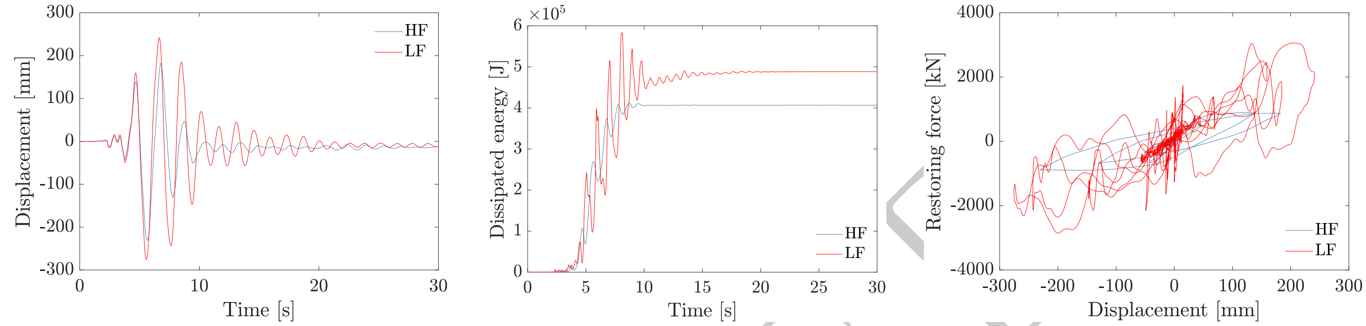

(a) (b) (c)

Figure 6: LF and HF simulations of the seismic response of Pier #11: a) displacement, b) dissipated energy, c) hysteresis loop.

The model is composed by a residual broad-band process (as done in [7]), and a modified version of the Mavroeidis, pulse model with random parameters [36],

$$V_{pul}\left(t\right) = \mathcal{M}_{pul}(t, \boldsymbol{X}_{pul}) = \left\{\frac{1}{2}V_p \cos\left[2\pi\left(\frac{t-T_{max,p}}{T_p}\right)+\nu\right] - \frac{D_r}{\gamma T_p}\right\}\left\{1+cos\left[\frac{2\pi}{\gamma}\left(\frac{t-T_{max,p}}{T_p}\right)\right]\right\},\ t_{i,p} < t \leq t_{f,p}. \tag{10}$$

where $\boldsymbol{X}_{pul} = [V_p, T_p, T_{max,p}, \gamma, \nu]$. Specifically, V_p and T_p are pulse amplitude and period, respectively, γ represents the number of oscillations within the pulse, ν is the phase angle shift w.r.t.the time modulation function, and $T_{max,p}$ is a location parameter for the peak of the excitation. D_r has been introduced in [20] to guarantee zero residual displacement at the end of the excitation, and it is defined as

$$D_r = V_p T_p \frac{\sin\left(\nu + \gamma\pi\right) - \sin\left(\nu - \gamma\pi\right)}{4\pi\left(1-\gamma^2\right)}. \tag{11}$$

Finally, $t_{i,p} = T_{max,p} - 0.5\gamma T_p$, and $t_{f,p} = T_{max,p} + 0.5\gamma T_p$ represent the start and the end of the pulse motion. While the pulse is modeled in the velocity domain, the residual is modelled in the acceleration domain, i.e., $a_{res}\left(t\right) = a\left(t\right) - \dot{v}_{pul}\left(t\right)^{*}$. Since the residual of the acceleration is a broadband motion, the model follows the same principles of [7], i.e.,

$$A_{res}\left(t\right) = \mathcal{M}_{res}(t, \boldsymbol{Z}|\boldsymbol{X}_{res}) = q\left(t|\,\boldsymbol{X}_q\right)\frac{h(t|\boldsymbol{X}_h) * W\left(t, \boldsymbol{Z}\right)}{\sigma_h\left(t, \boldsymbol{Z}|\,\boldsymbol{X}_h\right)}, \tag{12}$$

where $*$ denotes time convolution; $\boldsymbol{X}_{res} = [\boldsymbol{X}_q, \boldsymbol{X}_h]$; $q\left(t|\,\boldsymbol{X}_q\right)$ is a parametric time modulating function with random parameters $\boldsymbol{X}_q$; $h(t|\boldsymbol{X}_h)$ is the impulse-response function of a linear filter with time varying random parameters, where $\boldsymbol{X}_h$ represents a set of time invariant parameters; $W(t, \boldsymbol{Z}) = \sum_n^{N_t} \delta(t-t_n)Z_n$ is a band-limited white noise process, where $\boldsymbol{Z} = [Z_1, ...Z_{N_t}]$ is a standard normal Gaussian vector; and $\sigma_h\left(t, \boldsymbol{Z}|\,\boldsymbol{X}_h\right)$ is the variance of the convoluted process (i.e., the numerator of Eq.12). The modulating function proposed in [20] for near-field motions is

$$q\left(t|\,\boldsymbol{X}_q\right) = \begin{cases} C\left(\frac{t}{T_{max,q}}\right)^{\alpha} &, 0 < t \leq t_{max,q} \\ C\exp\left[-\beta\left(t - T_{max,q}\right)\right] &, t_{max,q} < t, \end{cases} \tag{13}$$

*lower case letter are used to indicate the single excitation; moreover, notice the time derivative on the pulse component.

Table 1: Selected events associated with the Emilia earthquake of May 29, 2012 (Italy).

Event ID	Time [h:m:s]	M_W	D [km]	Station code	Latitude [deg]	Longitude [deg]
IT-2012-0011	07:00:02	6	4.1	MRN	44.878231	11.061743
IT-2012-0011	07:00:02	6	4.1	MIRE	44.878212	11.061747
IT-2012-0011	07:00:02	6	9.3	T0814	44.793300	10.969200
IT-2012-0011	07:00:02	6	4.5	MIRH	44.882400	11.063100
IT-2012-0011	07:00:02	6	5.1	MIR02	44.886948	11.073198
IT-2012-0011	07:00:02	6	0.5	MIR01	44.844042	11.071316
IT-2012-0011	07:00:02	6	11.2	MIR03	44.938400	11.104500
IT-2012-0011	07:00:02	6	13	MIR04	44.927433	11.178312
IT-2012-0010	10:55:56	5.5	6.8	T0819	44.887300	10.898700
IT-2012-0011	07:00:02	6	11.3	T0813	44.877800	11.199200
IT-2012-0011	07:00:02	6	14.4	T0800	44.848600	11.247900
IT-2012-0011	07:00:02	6	6.1	SAN0	44.838000	11.143000
IT-2012-0011	07:00:02	6	8.6	MIR08	44.916900	11.089500
IT-2012-0011	07:00:02	6	9.9	T0802	44.875000	11.181600
IT-2012-0011	07:00:02	6	10.7	T0818	44.934800	11.030400
IT-2012-0011	07:00:02	6	14.3	T0811	44.783800	11.226500

where $\boldsymbol{X}_q = [\alpha, \beta, C, T_{max_q}]$ are the parameters of the function. Specifically, α and β are shape parameters controlling the ramping and decreasing phase of the residual, C is a scale factor, and $T_{max,q}$ is a location parameter defining the peak of the residual excitation. Moreover, it can be shown that a one-to-one mapping exists between these parameters and $D_{5-95,I_{a,res}} = T_{95,I_{a,res}} - T_{5,I_{a,res}}$, $T_{30,I_{a,res}}$, and $I_{a,res}$—where $T_{p,I_{a,res}}$ is the time corresponding to the p % of the cumulative Arias intensity of the residual, $I_{a,res}$. It follows that $\boldsymbol{X}_q$ can be written as $\boldsymbol{X}_q = [I_{a,res}, T_{30,I_{a,res}}, D_{5-95,I_{a,res}}]$. The filter is defined by

$$h(t|\boldsymbol{X}_h) = \frac{\omega_f(t)}{\sqrt{1-\zeta_f^2}} \exp\left[-\omega_f(t)\,\zeta_f \cdot t\right] \sin\left[\omega_f(t)\sqrt{1-\zeta_f^2} \cdot t\right]. \tag{14}$$

In Eq.14, the main frequency, $\omega_f(t)$, is evolving with time linearly. Specifically, $\omega_f(t) = \omega_{mid} + \dot{\omega}\,(t - T_{30;I_a})$, where ω_{mid} is the frequency at time $T_{30;I_{a_{res}}}$ (i.e., at 30 % of the cumulative Arias intensity of the residual) and $\dot{\omega}$ is the rate of change of the frequency with time. The damping of the filter, ζ_f, is considered time invariant. It follows that $\boldsymbol{X}_h = [\omega_{mid}, \dot{\omega}, \zeta]$. For further details the reader should refer to [20]. Finally, the artificial ground motion model can be written as

$$A(t) = \mathcal{M}_a(t, \boldsymbol{Z}|\boldsymbol{X}_a) = \mathcal{M}_{res}(t, \boldsymbol{Z}|\boldsymbol{X}_{res}) + \dot{\mathcal{M}}_{pul}(t, \boldsymbol{X}_{pul}) = A_{res}(t) + \dot{V}_{pul}(t), \tag{15}$$

where $\boldsymbol{X}_a = [\boldsymbol{X}_{res}, \boldsymbol{X}_{pul}]$.

In order to find parameter ranges consistent with the seismic hazard characteristic of the site, the artificial ground motion model was calibrated against real seismic records following the procedure explained in [20]. In detail, the seismic records of real events were selected based on the disaggregation analysis of the PGA with probability of exceedance of 2 % in 50 years [37]. Then, it was found that only pulse-like ground motions were likely to cause damage to the structure. Consequently, only pulse-like motions were retained and used for the calibration of the artificial ground motion model. It follows that the analysis and the result of this case study focus on pulse-like excitations. Table 1 reports the list of the 16 selected events, whose corresponding accelerograms were downloaded from the ITACA database [32]. All events belong to the Emilia earthquake occurred on May 29, 2012 (Italy). Each of the 16 events listed in Table 1 comprise N-S and E-W acceleration records, which were decomposed into principal components as explained in [38]. Velocity pulses where found on 12 over 16×2 components only, which were retained for the calibration. Figure 7 reports displacement, velocity and acceleration response spectra of the 12 retained components as well as the response spectra of the SLS and ULS accelerograms used for the RETRO experimental campaign. The response spectra of the selected records, which correspond to the gray lines, fall within the range established by the response spectra of SLS and ULS accelerograms adopted during experiments and, therefore, utilized to calibrate the HF simulator of the Rio Torto Bridge. The artificial ground motion model with pulse-like motion was calibrated for each of the 12 retained records following the procedure described in [20]. The parameter estimates are reported in Table 2.

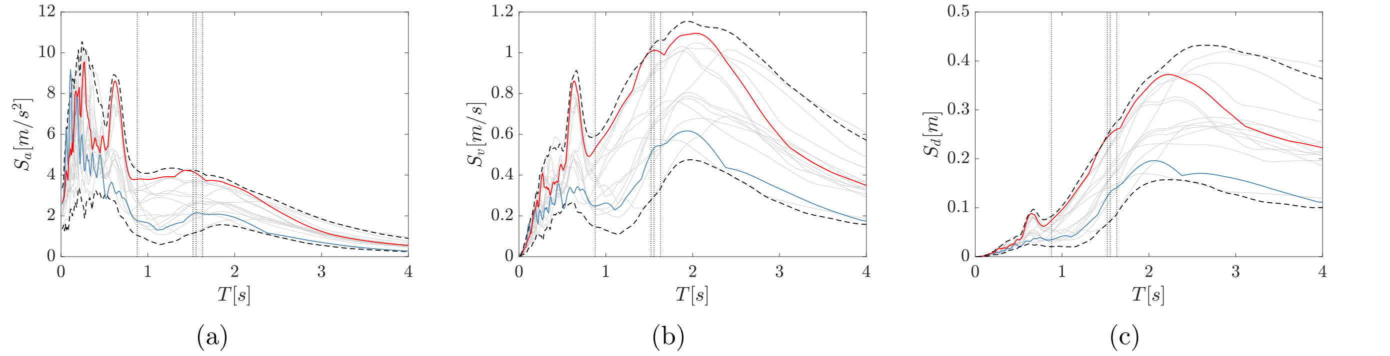

Figure 7: Selected records with pulse-like components: a) acceleration; b) velocity; c) displacement response spectra. Grey lines refer to single retained records with pulse-like component whereas black dashed lines indicate the corresponding 95 % confidence interval. Blue and red lines indicate SLS and ULS records used for the HS campaign, respectively. The periods of the first five eigenmodes of the Rio Torto Bridge estimated with the HF simulator are also reported.

Table 2: Parameters of Dabaghi's model identified on the pulse-like motions. min and max bounds, average values μ, standard deviations σ and coefficients of variations CoV are computed over the 12 selected records.

Record	V_p	T_p	ν	γ	$t_{max,p}$	$I_{a,res}$	$T_{30,I_{a,res}}$	$D_{5-95,I_{a,res}}$	ω_{mid}	$\dot{\omega}$	ζ
1	0.282	2.094	1.272	2.906	2.739	1.029	2.040	7.095	29.327	0.823	0.338
2	0.282	2.197	3.262	2.348	2.133	0.777	2.260	7.490	33.884	0.950	0.444
3	0.292	2.072	1.302	2.893	2.546	0.932	1.975	7.020	25.006	0.493	0.304
4	0.276	2.139	3.327	2.434	1.947	0.619	2.105	7.115	23.464	1.264	0.405
5	0.303	2.334	1.409	2.831	2.615	0.515	2.070	7.040	20.953	0.472	0.423
6	0.249	2.394	2.985	2.491	1.834	0.297	2.055	7.465	19.566	1.368	0.579
7	0.363	2.602	3.507	2.449	2.580	0.897	2.270	7.265	39.586	0.135	0.585
8	0.196	2.425	1.687	2.917	3.251	0.716	2.385	7.890	43.533	-0.344	0.462
9	0.392	2.282	4.530	2.350	2.862	0.881	2.305	7.185	32.215	0.212	0.306
10	0.292	1.949	2.616	2.339	1.472	0.408	1.530	4.195	23.015	1.948	0.408
11	0.218	1.762	3.069	2.418	1.748	0.335	1.390	3.115	33.868	0.949	0.378
12	0.205	2.688	1.924	2.212	3.352	0.298	2.025	6.720	30.052	-0.875	0.349
min	0.196	1.762	1.272	2.212	1.472	0.297	1.390	3.115	19.566	-0.875	0.304
max	0.392	2.688	4.530	2.917	3.352	1.029	2.385	7.890	43.533	1.948	0.585
μ	0.279	2.245	2.574	2.549	2.423	0.642	2.034	6.633	29.539	0.616	0.415
σ	0.056	0.254	1.001	0.249	0.573	0.255	0.286	1.378	7.159	0.742	0.089
CoV	0.201	0.113	0.389	0.098	0.236	0.398	0.141	0.208	0.242	1.203	0.214

Figure 8 compares 50 realizations of artificial records to the reference real record (with parameters listed in the second entry of Table 2).

6 Seismic fragility analysis of the bridge

Consistently with the notation introduced in the previous sections, input variables and QoIs of for the fragility analysis read,

$$\boldsymbol{Y}_{LF,p} = \{u_{p,1}, \dots, u_{p,12}\} \text{ , } \boldsymbol{X} \equiv \boldsymbol{X}_a = \{V_p, T_p, \gamma, \nu, T_{max,p}, I_{a,res}, T_{30,I_{a,res}}, D_{5-95,I_{a,res}}, \omega_{mid}, \zeta\} \tag{16}$$

where $u_{p,i}$ represents the p-quantile of the peak of the lateral drift of pier i-th. A GSA of pier lateral drift was performed to retain only the relevant parameters of the artificial ground motion model. In the proposed example, the evaluation cost of a single run of the HF structural simulator is about 10 min, that is, about 30 times larger than the evaluation cost of the LF simulator. Moreover, the evaluation of a QoI quantile relies on the evaluation of the structural simulator response for 100 realizations of baseline noise of the artificial ground motion model. Accordingly, PCE-based Sobol' sensitivity indices were computed for the LF simulator of the bridge. An initial ED of 200 samples was evaluated considering pier drift quantiles $\mathcal{P} = \{0.05 : 0.05 : 0.95\}$,

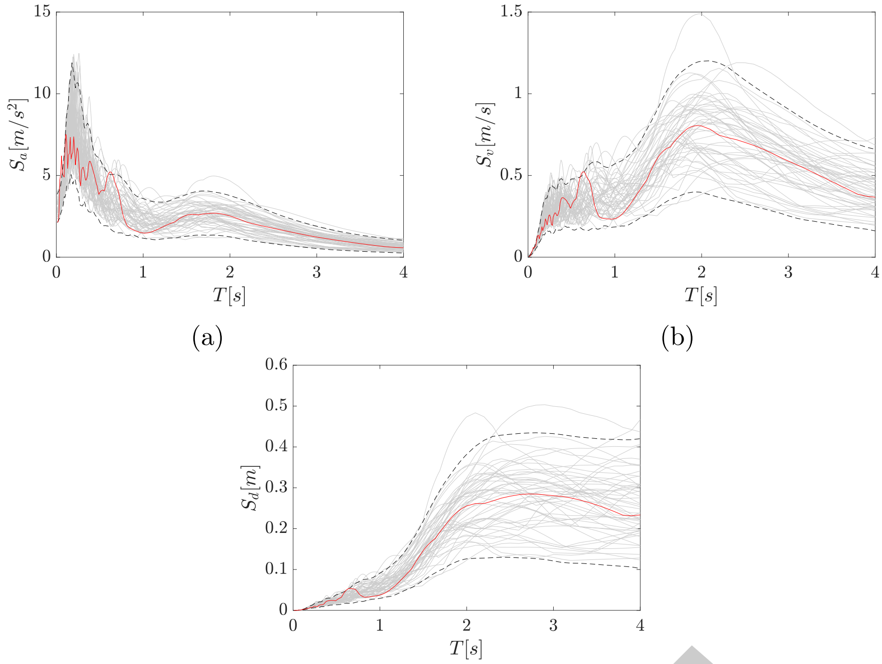

Figure 8: Response spectra of 50 realizations of the artificial ground motion model calibrated against the second record of Table 2: a) acceleration; b) velocity; c) displacement response spectra. Red lines refer to the reference record, grey lines represent the 50 realizations of the artificial ground motion model, and black dashed lines indicate the corresponding 95 % confidence interval.

Table 3: First-order Sobol' indices of lateral drift peak of Pier #11 (QoI).

$\mathcal{P}$	ϵ_{loo}	V_p	T_p	γ	ν	$t_{max,p}$	$I_{a,res}$	$T_{30,I_{a,res}}$	$D_{5-95,I_{a,res}}$	ω_{mid}	ζ
0.100	0.026	0.506	0.416	0.014	0.000	0.000	0.000	0.002	0.000	0.001	0.000
0.200	0.011	0.514	0.412	0.019	0.000	0.000	0.002	0.001	0.000	0.004	0.001
0.300	0.012	0.520	0.410	0.017	0.001	0.000	0.005	0.000	0.000	0.007	0.002
0.400	0.010	0.534	0.381	0.016	0.000	0.000	0.016	0.000	0.000	0.013	0.004
0.500	0.012	0.537	0.362	0.016	0.000	0.001	0.026	0.000	0.000	0.017	0.009
0.600	0.012	0.545	0.332	0.014	0.000	0.001	0.040	0.000	0.001	0.023	0.012
0.700	0.012	0.547	0.298	0.014	0.000	0.000	0.055	0.000	0.003	0.032	0.018
0.800	0.012	0.539	0.265	0.013	0.000	0.000	0.078	0.000	0.006	0.039	0.023
0.900	0.026	0.520	0.214	0.016	0.001	0.000	0.115	0.000	0.010	0.052	0.040

according to step 2 of the proposed framework. Such task entailed 20,000 evaluations of the LF simulator, that is, about 6,667 min of computational cost. Since GSA is used to uncover the inner working of the simulator, in this stage, it is legitimate to assume that all input variables are independently distributed. Tables 3 and 4 report PCE-based first-order and total Sobol' sensitivity indices related to the lateral drift of Pier #11 for the quantiles $\mathcal{P} = \{0.1 : 0.1 : 0.9\}$. Leave-one-out errors ϵ_{loo}, which are also reported, highlight fairly accurate PCEs. Similar errors were obtained up to 0.99 quantiles for all piers. It is noteworthy that, for regression-based PCE, the calculation of leave-one-out errors requires the evaluation of a single surrogate model based on the entire ED [39]. The contribution of V_p, T_p, $I_{a,res}$, ω_{mid} and ζ to the variability of drift quantiles was systematically dominant for all piers. Constant average values reported in Table 2 were considered for all other parameters in the following calculations. Among retained parameters, univariate effects highlighted monotonic increasing relationships with the QoI for V_p, $I_{a,res}$ and ζ only. The results of Figure 9 refer to Pier #11 but the same trend was systematically observed for all piers. Accordingly, V_p and $I_{a,res}$ were employed as IMs for computing the fragility analysis. Following step 3 of the framework, a refined ED of 10 samples was evaluated using the HF simulator of the bridge considering,

$$\boldsymbol{X}_\alpha = \{V_p, T_p, I_{a,res}, \omega_{mid}, \zeta\}, \tag{17}$$

$$\boldsymbol{x}_\beta = E\left[\{\gamma, \nu, T_{max,p}, T_{30,I_{a,res}}, D_{5-95,I_{a,res}}, \omega_{mid}\}\right]. \tag{18}$$

Table 4: Total Sobol' indices of lateral drift peak of Pier #11 (QoI).

$\mathcal{P}$	ϵ_{loo}	V_p	T_p	γ	ν	$t_{max,p}$	$I_{a,res}$	$T_{30,I_{a,res}}$	$D_{5-95,I_{a,res}}$	ω_{mid}	ζ
0.100	0.026	0.539	0.471	0.024	0.002	0.001	0.012	0.003	0.000	0.005	0.007
0.200	0.011	0.536	0.448	0.031	0.002	0.003	0.010	0.003	0.003	0.011	0.006
0.300	0.012	0.536	0.435	0.028	0.003	0.003	0.012	0.002	0.005	0.015	0.009
0.400	0.010	0.546	0.408	0.026	0.001	0.002	0.024	0.001	0.002	0.021	0.008
0.500	0.012	0.549	0.388	0.027	0.000	0.003	0.033	0.000	0.000	0.021	0.012
0.600	0.012	0.555	0.358	0.023	0.002	0.002	0.048	0.001	0.002	0.029	0.017
0.700	0.012	0.554	0.323	0.025	0.001	0.003	0.062	0.002	0.004	0.040	0.022
0.800	0.012	0.547	0.287	0.022	0.001	0.005	0.090	0.001	0.011	0.048	0.027
0.900	0.026	0.526	0.230	0.025	0.005	0.004	0.124	0.003	0.012	0.060	0.046

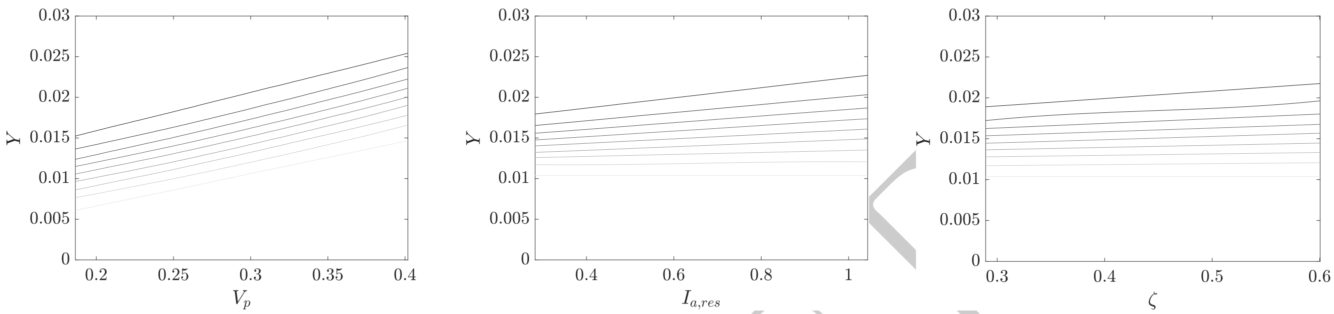

(a) (b) (c)

Figure 9: Univariate effects for the lateral drift peak of Pier #11 (QoI) for the quantiles reported in Tables 3 and 4. Lighter curves refer to quantile $p = 0.1$ while darker curves refer to quantile $p = 0.9$.

For each sample of the refined ED, 100 baseline noise realizations were considered entailing a total of 1,000 evaluations of the HF structural simulator, that is, about 10,000 min of computational time. Then, HK surrogates were trained for different ED sizes. Accordingly, HF-n indicates a HK surrogate computed with n samples of the HF structural simulator response quantiles. Following step 3 of the framework, the PCE surrogate trained on the LF simulator was used as a trend function for the HK surrogates. A Matérn 5/2 correlation function $R\left(\boldsymbol{X} - \boldsymbol{X}'|\boldsymbol{\theta}\right)$ and second-order polynomial trend function $\boldsymbol{\mu}\left(\boldsymbol{X}\right)$ were adopted.

According to step 4 of the framework, the fragility models reported in Figures 10 and 11 were computed via Monte-Carlo-based UQ forward analysis using surrogate models and an EDP drift threshold value $\bar{y} = 0.01$. This value corresponds to a medium damage state characterized by the onset of concrete spalling in the transverse beams, as demonstrated in [34, 40, 41] by means of numerical simulations and experimental tests. Specifically, the fragility curves reported in Figure 10 were obtained from the PCE surrogate of the LF simulator and three HK surrogates of the HF simulator. In the latter case, the three HK surrogates were obtained considering 8, 9, and 10 samples of the HF simulator response; hence, they are indicated as HF-8, HF-9, and HF-10, respectively. The red shaded area indicates the 95 % confidence interval of the fragility curve computed with the HF-10 HK surrogate. As can be observed, fragility curves approach a stable shape already with 8 samples of the HF simulator response. The motivation behind the selection of V_p as IM for the fragility curves is twofold. First, V_p is associated with the larger Sobol' sensitivity index and, therefore, it is the most sensitive parameter of the LF simulator (see Tables 3 and 4 in this regard). Moreover, according to Figure 9a, V_p shows a monotonic increasing relationship with the selected EDP. On the other hand, the fragility surface of Figure 11 was obtained for the HK surrogate indicated as HF-10. Owing to their substantial contribution to the variability of the EDP demonstrated by Sobol' indices, V_p and $I_{a,res}$ were selected as IMs. Moreover, according to Figure 9, both these two parameters show a monotonic increasing relationship with the EDP. In order to demonstrate the accuracy of the proposed framework, both fragility models were compared to crude Monte Carlo estimates of the failure probability of the HF simulator computed for two validation points. In this regard, the red diamonds of Figures 10 and 11 indicate mean value and 95 % confidence interval of failure probability estimates obtained with 100 samples[*] of the HF simulator response—i.e., circa 1,000 min per point of computational time. In detail, the validation point for the fragility curve (Figure 10) assumes $V_p = 0.3$ while the validation point for the

[*] Notice that with 100 simulations the mean estimate is stable, while the confidence bounds should be considered as indicative

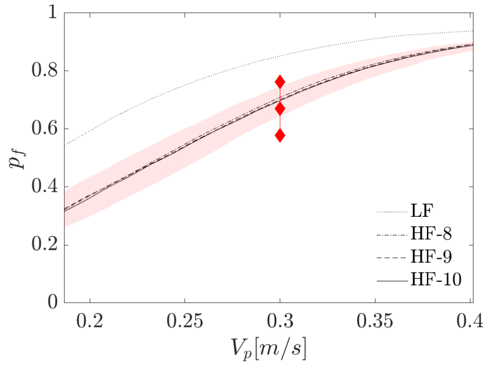

Figure 10: Fragility curves for the lateral drift peak of Pier #11 (QoI).

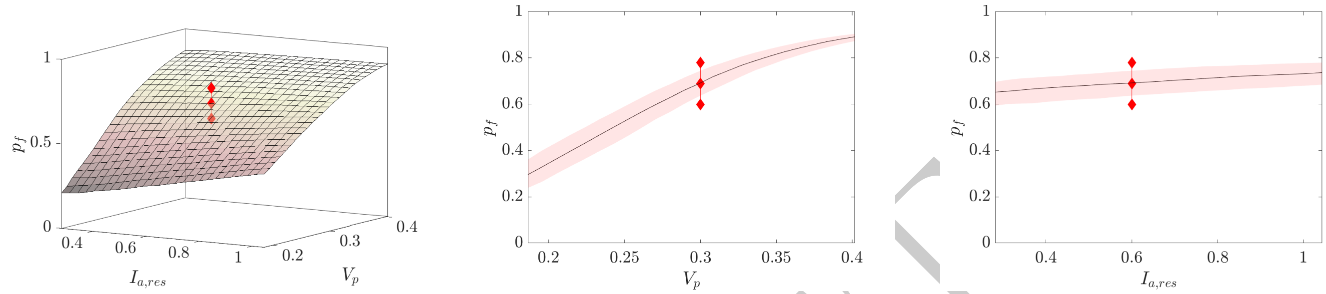

(a) (b) (c)

Figure 11: Fragility surface for the lateral drift peak of Pier #11 (QoI): a) fragility surface; b) section along V_p; c) section along $I_{a,res}$.

fragility surface (Figure 11) assumes $V_p = 0.3$ and $I_{a,res} = 0.6$. For the sake of clarity, two orthogonal sections of the fragility surface intersecting the validation point are also included in Figure 11. For both fragility models, Monte Carlo estimates are consistent with fragility model predictions.

Although HK surrogates were obtained assuming independent uniformly distributed ground motion parameters, fragility models can be easily re-sampled considering a joint PDF calibrated for the specific seismic hazard. Also, provided with such simulation framework, ground motion parameters can be mapped to instrumental IM as illustrated in [30].

7 Conclusions

This study introduced a computational framework for efficient and accurate seismic fragility analysis based on a combination of artificial ground motions and surrogate modeling of multiple stochastic simulators characterized by different levels of fidelity. The effectiveness of the proposed framework is demonstrated throughout a benchmark case study, which consists of a reinforced concrete bridge vulnerable to ground motions with pulse-like components. Specifically, surrogate modeling is applied at the level of quantiles of a scalar response quantity of interest, which is evaluated either with an expensive-to-evaluate high-fidelity or a cheaper low-fidelity stochastic simulator. As a result, two fragility models associated with a medium damage state are computed for the lateral drift of one pier of the bridge based on $1,000$ evaluations of the high-fidelity simulator plus $20,000$ evaluations of the low-fidelity simulator. Accuracy of failure probability estimates is demonstrated by comparison with Monte Carlo simulations of the high-fidelity simulator. The main findings of the benchmark study, which can be reasonably generalized to seismic fragility analysis of bridges, are that:

- 100 artificial ground motions are sufficient to attain fairly accurate quantile estimates in the range $0.05 - 0.95$ for a given sample of the stochastic simulator parameters (both low- and high-fidelity).
- Polynomial-chaos-based global sensitivity analysis facilitates the selection of the important parameters of the artificial ground motion model to be used as intensity measures for the fragility analysis.
- Dynamic substructuring and hierarchical kriging provide a mathematically sound framework for balancing computational cost and accuracy of structural analysis.

It is critical to remark that the domain of validation of the high-fidelity simulator defines the perimeter of any validated output of the framework. An important future research direction that directly builds upon this framework is the optimal design of experimental campaigns to meet a target degree of accuracy of fragility models.

Appendix A. PCE-based Sobol' sensitivity indices

Assume that the vector of input variables $\boldsymbol{X}$ has support $\mathcal{D}_{\boldsymbol{X}}$ and follows an independent joint PDF $f_{\boldsymbol{X}}(\boldsymbol{X}) = \prod_m^M f_{X_m}(x_m)$ where f_{X_m} is the marginal PDF of the m-th input variable. Any square-integrable mapping $Y = \mathcal{M}(\boldsymbol{X})$ w.r.t. the probability measure associated with $f_{\boldsymbol{X}}$, can be written as a sum of functions of increasing dimension as [42]:

$$\mathcal{M}(\boldsymbol{X}) = \mathcal{M}_0 + \sum_{m=1}^{M} \mathcal{M}_m(X_m) + \sum_{1 \leq m \leq l \leq M} \mathcal{M}_{m,l}(X_m, X_l) + \ldots + \mathcal{M}_{1,2,\ldots,M}(\boldsymbol{X}), \tag{A.1}$$

or equivalently:

$$\mathcal{M}(\boldsymbol{X}) = \mathcal{M}_0 + \sum_{\boldsymbol{u} \neq \emptyset} \mathcal{M}_{\boldsymbol{u}}(\boldsymbol{X}_{\boldsymbol{u}}), \tag{A.2}$$

where $\mathcal{M}_0$ is the mean value of Y, $\boldsymbol{u} = \{m_1, \ldots, m_s\} \subset \{1, \ldots, M\}$ are index sets, and $\boldsymbol{X}_{\boldsymbol{u}}$ denotes a subvector of $\boldsymbol{X}$ containing only the components indexed by $\boldsymbol{u}$. The number of summands in the above equation is $2^M - 1$. The uniqueness and orthogonality of Sobol'-Hoeffding decomposition allow for the following decomposition of the variance D of Y:

$$D = \mathrm{Var}\left[\mathcal{M}(\boldsymbol{X})\right] = \sum_{\boldsymbol{u} \neq \emptyset} \mathcal{D}_{\boldsymbol{u}} \tag{A.3}$$

where $\mathcal{D}_{\boldsymbol{u}}$ denotes the partial variance:

$$\mathcal{D}_{\boldsymbol{u}} = \mathrm{Var}\left[\mathcal{M}_{\boldsymbol{u}}(\boldsymbol{X}_{\boldsymbol{u}})\right] = \mathbb{E}\left[\mathcal{M}_{\boldsymbol{u}}^2(\boldsymbol{X}_{\boldsymbol{u}})\right]. \tag{A.4}$$

The Sobol' index $S_{\boldsymbol{u}}$ can be defined as the fraction of the total variance $D_{\boldsymbol{u}}$ that corresponds to the set of input variables indexed by $\boldsymbol{u}$:

$$S_{\boldsymbol{u}} = \frac{D_{\boldsymbol{u}}}{D}. \tag{A.5}$$

By construction, $\sum_{\boldsymbol{u} \neq \emptyset} S_{\boldsymbol{u}} = 1$. First-order indices $S_m^{(1)}$ describe the influence of each parameters X_m considered separately. Second-order indices $S_{ml}^{(2)}$ describe the influence from pairs of parameters $\{X_m, X_l\}$ not already accounted for by X_m or X_l separately. High-order indices describe combine influences from larger sets of parameters. The total sensitivity indices $S_m^{(\mathrm{tot})}$ represent the total effect of an input variable X_m accounting for its main effect and all interactions with other input variables. It follows that $S_m^{(\mathrm{tot})} = 1 - S_{\sim m}$, where $S_{\sim m}$ is the sum of all $S_{\boldsymbol{u}}$ with $\boldsymbol{u}$ not including m. Sobol' indices can be evaluated by Monte Carlo simulation [43], which requires $\mathcal{O}(10^3)$ model evaluations for each index $S_{\boldsymbol{u}}$. Sobol' indices can be obtained analytically at no additional cost than computing the PCE. A concise description of PCE-based Sobol' sensitivity indices estimation is given herein; for further details, the reader is referred to [44, 45].

PCE relies on the decomposition of $Y = \mathcal{M}(\boldsymbol{X})$, as a linear superposition of non-linear functions as follows:

$$\widehat{Y} = \mathcal{M}^{\mathrm{PCE}}(\boldsymbol{X}) = \sum_{\boldsymbol{\alpha} \in \mathcal{A}} y_{\boldsymbol{\alpha}} \Psi_{\boldsymbol{\alpha}}(\boldsymbol{X}), \tag{A.6}$$

where $\{\Psi_{\boldsymbol{\alpha}}, \boldsymbol{\alpha} \in \mathcal{A}\}$ is a set of multivariate polynomials that are orthogonal w.r.t. the input vector with independent components $\boldsymbol{X} \sim f_{\boldsymbol{X}}(\boldsymbol{X}) = \prod_{m=1}^M f_{\boldsymbol{X}_m}(\boldsymbol{X}_m)$, $\boldsymbol{\alpha} = (\alpha_1, \ldots \alpha_M)$ is a multi-index that identifies the polynomial degree in each of the input variables, and $y_{\boldsymbol{\alpha}}$ denotes the corresponding polynomial coefficient (coordinate). Following the orthonormality condition, $\mathbb{E}\left[\mathcal{M}^{\mathrm{PCE}}(\boldsymbol{X})\right] = y_{\boldsymbol{0}}$. For practical purposes, the infinite sum in Eq.A.6 needs to be truncated to a finite series. This is commonly achieved by maximum-degree or hyperbolic norm truncation (for more details, see [21]). In order to compute the PCE, first, a so-called ED, consisting of a set of realization of the input vector $\boldsymbol{\mathcal{X}} = \{\boldsymbol{x}^{(1)}, \ldots, \boldsymbol{x}^{(N)}\}$ and the corresponding model evaluations $\mathcal{Y} = \{y^{(1)}, \ldots, y^{(N)}\}$, is generated. Then, the set of coefficients $\boldsymbol{y_\alpha}$ is estimated by minimizing the expected mean-square approximation error on the ED by solving:

$$\widehat{\boldsymbol{y}}_{\boldsymbol{\alpha}} = \arg\min_{\boldsymbol{y}_{\boldsymbol{\alpha}}} \mathbb{E}\left[\left(Y - \widehat{Y}\right)^2\right] \tag{A.7}$$

In the present application, the ED was formed by sampling the input variable space with a Sobol' low-discrepancy sequence. The minimization in Eq.A.7 was solved using the hybrid least angle regression method originally proposed in [21]. It is straightforward to obtain the Sobol' decomposition of Y in an analytical form by observing that the summands $\mathcal{M}_{\boldsymbol{u}}^{\mathrm{PCE}}\left(\boldsymbol{X}_{\boldsymbol{u}}\right)$ in Eq.A.2 can be written as:

$$\mathcal{M}_{\boldsymbol{u}}^{\mathrm{PCE}}\left(\boldsymbol{X}_{\boldsymbol{u}}\right) = \sum_{\boldsymbol{\alpha}\in\mathcal{A}_{\boldsymbol{u}}} y_{\boldsymbol{\alpha}} \boldsymbol{\Psi}_{\boldsymbol{\alpha}}\left(\boldsymbol{X}_{\boldsymbol{u}}\right), \tag{A.8}$$

where $\mathcal{A}_{\boldsymbol{u}} = \{\boldsymbol{\alpha} \in \mathcal{A} : \alpha_k \neq 0 \text{ if and only if } k \in \boldsymbol{u}\}$ denotes the set of multi-indices such that $\cup\mathcal{A}_{\boldsymbol{u}} = \mathcal{A}$. Consequently, due to the uniqueness of Sobol'-Hoeffding decomposition, there is an analytical expression of $\mathcal{M}_{\boldsymbol{u}}^{\mathrm{PCE}}$ of Eq.A.8, which serves as a proxy of $\mathcal{M}_{\boldsymbol{u}}$. The analytical expression of the total variance of a PCE is given by [46]:

$$D = \mathrm{Var}\left[\mathcal{M}^{\mathrm{PCE}}\left(\boldsymbol{X}\right)\right] = \sum_{\boldsymbol{\alpha}\in\mathcal{A}} y_{\boldsymbol{\alpha}}^2. \tag{A.9}$$

Similarly, the partial variance $D_{\boldsymbol{u}}$ reads:

$$D_{\boldsymbol{u}} = \mathrm{Var}\left[\mathcal{M}_{\boldsymbol{u}}^{\mathrm{PCE}}\left(\boldsymbol{X}_{\boldsymbol{u}}\right)\right] = \sum_{\boldsymbol{\alpha}\in\mathcal{A}_{\boldsymbol{u}}} y_{\boldsymbol{\alpha}}^2. \tag{A.10}$$

Accordingly, the Sobol' indices of any order can be approximated by a simple combination of the squares of the PCE coefficients by substituting Eqs.A.10 and A.9 in Eq.A.5. For instance, the first-order Sobol' indices, which describe the influence of each input variable $\boldsymbol{X}_m$ considered separately, read:

$$S_m^{(1)} = \frac{\sum_{\boldsymbol{\alpha}\in\mathcal{A}_m} y_{\boldsymbol{\alpha}}^2}{\sum_{\boldsymbol{\alpha}\in\mathcal{A}} y_{\boldsymbol{\alpha}}^2}\ ,\ \mathcal{A}_m = \{\boldsymbol{\alpha} \in \mathcal{A} : \alpha_m > 0\ ,\ \alpha_{m\neq l} = 0\} \tag{A.11}$$

whereas the total Sobol' indices, which represent the total effect of an input variable $\boldsymbol{X}_m$ accounting for its main effect and all interaction with other input variables, are given by:

$$S_m^{(\mathrm{tot})} = \frac{\sum_{\boldsymbol{\alpha}\in\mathcal{A}_m^{\mathrm{tot}}} y_{\boldsymbol{\alpha}}^2}{\sum_{\boldsymbol{\alpha}\in\mathcal{A}} y_{\boldsymbol{\alpha}}^2}\ ,\ \mathcal{A}_m^{\mathrm{tot}} = \{\boldsymbol{\alpha} \in \mathcal{A} : \alpha_m > 0\}. \tag{A.12}$$

Sobol' indices provide quantitative insight on the importance of an input variable. However, they do not include information about the direction in which an input variable affects the model response Y. So-called univariate effects can answer this question [47, 48]. A univariate effect is the expectation of Y conditioned to the value of a single input variable. Univariate effects have a closed analytical form for PCE models, closely related to the first-order Sobol' decomposition,

$$\mathcal{M}_m^{(1)}\left(X_m\right) = \sum_{\boldsymbol{\alpha}\in\mathcal{A}_m} y_{\boldsymbol{\alpha}} \Psi_{\boldsymbol{\alpha}}\left(X_m\right)\ ,\ \mathcal{A}_m = \{\boldsymbol{\alpha} \in \mathcal{A} : \alpha_m > 0, \alpha_{m\neq l} = 0\} \tag{A.13}$$

In this study, computations of both PCE and Sobol' indices were performed using UQLab, which is a MATLAB toolbox for UQ developed by the Chair of Risk, Safety and Uncertainty Quantification of ETH Zurich [49, 50, 51].

Appendix B. HK surrogate modeling

Let $\{\mathcal{M}_c,\ c = 1, \ldots C\}$ being a series of simulators sorted by increasing level of fidelity, and y_c the associated output, $y_c = \mathcal{M}_c(\boldsymbol{x})$. In addition, let $\hat{\mathcal{M}}_c^K$ define the Kriging surrogate model of the simulator $\mathcal{M}_c(\boldsymbol{x})$. A Kriging surrogate model is defined as an infinite collection of jointly Gaussian random variables (i.e., a Gaussian stochastic process). Any finite sample of the process is a Gaussian random vector, which is completely defined by the multivariate Gaussian distribution [52]. In this context, the input $\boldsymbol{X}$ is sampled at N_c distinct locations within the support $\mathcal{D}_{\boldsymbol{X}}$, and the corresponding scalar output are $\left\{y_c^{(n)} = \mathcal{M}_c\left(\boldsymbol{x}_c^{(n)}\right), n = 1, \ldots, N_c\right\}$. The N_c distinct input samples are collected in the set $\boldsymbol{\mathcal{X}}_c = \left\{\boldsymbol{X}^{(1)}, \ldots, \boldsymbol{X}^{(N_c)}\right\}^T$ and the output in the set $\boldsymbol{\mathcal{Y}}_c = \left\{y_c^{(1)}, \ldots, y_c^{(N_c)}\right\}^T$. Here, the set $\boldsymbol{\mathcal{Y}}_c$ is considered as realization of a Gaussian random vector, $\boldsymbol{Y}_c = \left[Y^{(1)}, \ldots, Y^{(N_c)}\right]^T$, with mean $\mu_c(\boldsymbol{X})$, and covariance matrix $\boldsymbol{\Sigma}_c(\boldsymbol{X})$. Therefore, the kriging surrogate model of the c simulator can be defined as [53, 54, 52]

$$\begin{aligned} \mathcal{M}_c(\boldsymbol{X}) \approx \hat{\mathcal{M}}_c^K(\boldsymbol{X}) &= \mu_c(\boldsymbol{X}) + \sigma_c^2 Z(\boldsymbol{X}), \\ &= \boldsymbol{f}_c(\boldsymbol{X})^T \boldsymbol{\beta}_c + \sigma_c^2 Z(\boldsymbol{X}), \end{aligned} \tag{B.1}$$

where $\boldsymbol{\beta}_c$ is a vector of regression coefficients, $\boldsymbol{f}_c(\boldsymbol{X})$ is a vector collecting a series of basis functions, σ_c^2 is the variance of the process, and $Z(\boldsymbol{X})$ is a zero-mean, unit-variance stationary Gaussian process. Therefore, $Z(\boldsymbol{X})$ is fully determined by the correlation function $R(\boldsymbol{X}, \boldsymbol{X}'|\boldsymbol{\theta}) = R(\boldsymbol{X} - \boldsymbol{X}'|\boldsymbol{\theta})$ between two distinct points $(\boldsymbol{X}, \boldsymbol{X}')$ in the input space, where $\boldsymbol{\theta}$ is a set of hyper-parameters. Given the input ED $\boldsymbol{\mathcal{X}}_c$ and the output set $\boldsymbol{\mathcal{Y}}_c$, $\boldsymbol{\beta}_c$, $\boldsymbol{\theta}_c$, and σ_c are generally determined by generalized least squares as follow [54, 55]:

$$\hat{\boldsymbol{\theta}}_c = \arg\min A_{\mathcal{D}_{\boldsymbol{\theta}}} \left[\frac{1}{2}\log\left(\det\left(\boldsymbol{R}\right)\right) + \frac{n}{2}\log\left(2\pi\sigma_c^2\right) + \frac{n}{2}\right], \tag{B.2}$$

$$\hat{\boldsymbol{\beta}}(\hat{\boldsymbol{\theta}}_c) = \left(\boldsymbol{F}_c^T \boldsymbol{R}^{-1} \boldsymbol{F}_c\right)^{-1} \boldsymbol{F}_c^T \boldsymbol{R}^{-1} \boldsymbol{\mathcal{Y}}_c, \tag{B.3}$$

$$\hat{\sigma}_c^2(\hat{\boldsymbol{\theta}}_c) = \frac{(\boldsymbol{\mathcal{Y}}_c - \boldsymbol{F}_c\hat{\boldsymbol{\beta}}_c)^T \boldsymbol{R}^{-1} (\boldsymbol{\mathcal{Y}}_c - \boldsymbol{F}_c\hat{\boldsymbol{\beta}}_c)}{N_c}, \tag{B.4}$$

where $R_{n,m} = \boldsymbol{R}(\boldsymbol{X}^n, \boldsymbol{X}^m)$ is the correlation matrix between the N_c samples, and $\boldsymbol{F}_c = [\boldsymbol{f}_c(\boldsymbol{X}^{(1)}), \ldots, \boldsymbol{f}_c(\boldsymbol{X}^{(N_c)})]^T$ is the information matrix. Next, given a desired test point $\boldsymbol{x}^*$, the random variable of the unobserved output $Y_c^*|\boldsymbol{\mathcal{X}}_c, \boldsymbol{\mathcal{Y}}_c = \mathcal{M}_c^K(\boldsymbol{x}^*|\boldsymbol{\mathcal{X}}_c, \boldsymbol{\mathcal{Y}}_c)$ has conditional Gaussian distribution [54] with parameters

$$\begin{aligned} \mu_{y_c^*} &= \mathbb{E}\left[Y_c^* \mid \boldsymbol{\mathcal{X}}_c, \boldsymbol{\mathcal{Y}}_c\right], \\ &= \boldsymbol{f}_c(\boldsymbol{x}^*)^T \hat{\boldsymbol{\beta}}_c + \boldsymbol{r}^T(\boldsymbol{x}^*) \boldsymbol{R}^{-1} \left(\boldsymbol{\mathcal{Y}}_c - \boldsymbol{F}_c \hat{\boldsymbol{\beta}}_c\right), \end{aligned} \tag{B.5}$$

$$\begin{aligned} \sigma_{y_c^*}^2 &= \mathrm{Var}\left[Y_c^* \mid \boldsymbol{\mathcal{X}}_c, \boldsymbol{\mathcal{Y}}_c\right], \\ &= \hat{\sigma}_c^2 \left[1 - \boldsymbol{r}^T(\boldsymbol{x}^*) \boldsymbol{R}^{-1} \boldsymbol{r}(\boldsymbol{x}^*) + \left(\boldsymbol{F}_c^T \boldsymbol{R}^{-1} \boldsymbol{r}(\boldsymbol{x}^*) - \boldsymbol{f}_c(\boldsymbol{x}^*)\right)^T \left(\boldsymbol{F}_c^T \boldsymbol{R}^{-1} \boldsymbol{F}_c\right)^{-1} \left(\boldsymbol{F}_c^T \boldsymbol{R}^{-1} \boldsymbol{r}(\boldsymbol{x}^*) - \boldsymbol{f}_c(\boldsymbol{x}^*)\right)\right], \end{aligned} \tag{B.6}$$

where $\boldsymbol{r}(\boldsymbol{x}^*) = \hat{\boldsymbol{\theta}}_c) = [R(\boldsymbol{x}^* - \boldsymbol{x}^{(1)}|\hat{\boldsymbol{\theta}}_c), \ldots, R(\boldsymbol{x}^* - \boldsymbol{x}^{(N_c)}|\hat{\boldsymbol{\theta}}_c)]^T$ is the cross-correlation vector between the point $\boldsymbol{x}^*$ and each of the points of $\boldsymbol{\mathcal{X}}_c$. In this study, we use a nested combination of surrogate models to define a HK surrogate [23]. Specifically, a PCE surrogate of the LF simulator is used as a trend for the HF simulator. For the two levels $c \in [LF, HF]$, the HK predictor at an unobserved point $\boldsymbol{x}^*$ can be written as [29]:

$$\mu_{y_{HF}^*} = \hat{\mathcal{M}}_{LF}^{PCE}(\boldsymbol{x}^*)\hat{\beta}_{HF} + \boldsymbol{r}(\boldsymbol{x}^*)^T \boldsymbol{R}^{-1}(\boldsymbol{\mathcal{Y}}_{HF} - \boldsymbol{F}_{LF}\hat{\beta}_{HF}), \tag{B.7}$$

where $\hat{\mathcal{M}}_{LF}^{PCE}(\boldsymbol{x}^*)$ is PCE surrogate of the LF simulator, $\boldsymbol{\mathcal{Y}}_{HF}$ is the vector of output from the HF simulator, $\boldsymbol{F}_{LF} = [\boldsymbol{\mathcal{M}}_{LF}(\boldsymbol{x}_1), \ldots, \boldsymbol{\mathcal{M}}_{LF}(\boldsymbol{x}_{N_c})]$, and $\hat{\beta}_{HF}$ is a constant. The variance of the HK predictor is similar to Eq.B.6, i.e.

$$\sigma_{y_{HF}^*}^2 = \hat{\sigma}_{HF}^2 \left[1 - \boldsymbol{r}(\boldsymbol{x}^*)^T \boldsymbol{R}^{-1} \boldsymbol{r}(\boldsymbol{x}^*) + \left(\boldsymbol{F}_{LF}^T \boldsymbol{R}^{-1} \boldsymbol{r}(\boldsymbol{x}^*) - \hat{\mathcal{M}}_{LF}^{PCE}(\boldsymbol{x}^*)\right)^T \left(\boldsymbol{F}_{LF}^T \boldsymbol{R}^{-1} \boldsymbol{F}_{LF}\right)^{-1} \left(\boldsymbol{F}_{LF}^T \boldsymbol{R}^{-1} \boldsymbol{r}(\boldsymbol{x}^*) - \hat{\mathcal{M}}_{LF}^{PCE}(\boldsymbol{x}^*\right. \tag{B.8}$$

In this study, computations of kriging surrogates were performed using UQLab, which is a MATLAB toolbox for UQ developed by the Chair of Risk, Safety and Uncertainty Quantification of ETH Zurich [49, 56].

Acknowledgments

The authors wish to acknowledge the Chair of Structural Dynamics and Earthquake Engineering (Prof. Dr. Božidar Stojadinović) and the Chair of Risk, Safety and UQ (Prof. Dr. Bruno Sudret) of ETH Zurich, Switzerland, for having supported this research.

References

[1] D. Vamvatsikos and C. Cornell, "Incremental dynamic analysis," *Earthquake Engineering & Structural Dynamics*, vol. 31, pp. 491 – 514, 2002.

[2] K. Porter, R. Kennedy, and R. Bachman, "Creating fragility functions for performance-based earthquake engineering," *Earthquake Spectra*, vol. 23, 2007.

[3] J. W. Baker, "Efficient analytical fragility function fitting using dynamic structural analysis," *Earthquake Spectra*, vol. 31, no. 1, pp. 579–599, 2015.

[4] H. Y. Noh, D. Lallemant, and A. S. Kiremidjian, "Development of empirical and analytical fragility functions using kernel smoothing methods," *Earthquake Engineering & Structural Dynamics*, vol. 44, no. 8, pp. 1163–1180, 2015.

[5] B. A. Bradley, "A critical examination of seismic response uncertainty analysis in earthquake engineering," *Earthquake Engineering & Structural Dynamics*, vol. 42, no. 11, pp. 1717–1729, 2013.

[6] V. Silva, S. Akkar, J. Baker, P. Bazzurro, J. M. Castro, H. Crowley, M. Dolsek, C. Galasso, S. Lagomarsino, R. Monteiro, D. Perrone, K. Pitilakis, and D. Vamvatsikos, "Current Challenges and Future Trends in Analytical Fragility and Vulnerability Modeling," *Earthquake Spectra*, vol. 35, no. 4, pp. 1927–1952, 2019.

[7] S. Rezaeian and A. Der Kiureghian, "A stochastic ground motion model with separable temporal and spectral nonstationarities," *Earthquake Engineering & Structural Dynamics*, vol. 37, no. 13, pp. 1565–1584, 2008.

[8] S. Rezaeian and A. Der Kiureghian, "Simulation of synthetic ground motions for specified earthquake and site characteristics," *Earthquake Engineering & Structural Dynamics*, pp. n/a–n/a, 2010.

[9] A. H. Schellenberg, S. A. Mahin, and G. L. Fenves, "Advanced Implementation of Hybrid Simulation," Tech. Rep. PERR 2009/104, Pacific Earthquake Engineering Research (PEER) Center, University of California, Berkeley, 2009.

[10] D. de Klerk, D. J. Rixen, and S. N. Voormeeren, "General Framework for Dynamic Substructuring: History, Review and Classification of Techniques," *AIAA Journal*, vol. 46, no. 5, pp. 1169–1181, 2008.

[11] C. Mai, K. Konakli, and B. Sudret, "Seismic fragility curves for structures using non-parametric representations," *Frontiers of Structural and Civil Engineering*, vol. 11, no. 2, pp. 169–186, 2017.

[12] I. Zentner, "A general framework for the estimation of analytical fragility functions based on multivariate probability distributions," *Structural Safety*, vol. 64, pp. 54–61, 2017.

[13] K. Trevlopoulos, C. Feau, and I. Zentner, "Parametric models averaging for optimized non-parametric fragility curve estimation based on intensity measure data clustering," *Structural Safety*, vol. 81, p. 101865, 2019.

[14] D. Altieri and E. Patelli, "An efficient approach for computing analytical non-parametric fragility curves," *Structural Safety*, vol. 85, p. 101956, 2020.

[15] I. Gidaris, A. A. Taflanidis, and G. P. Mavroeidis, "Kriging metamodeling in seismic risk assessment based on stochastic ground motion models: Seismic Risk Assessment Through Kriging Metamodeling," *Earthquake Engineering & Structural Dynamics*, vol. 44, no. 14, pp. 2377–2399, 2015.

[16] S. Ghosh, A. Roy, and S. Chakraborty, "Kriging Metamodeling-Based Monte Carlo Simulation for Improved Seismic Fragility Analysis of Structures," *Journal of Earthquake Engineering*, pp. 1–21, 2019.

[17] F. Paolacci, F. J. Molina, R. Giannini, L. Di Sarno, G. Abbiati, A. Mohamad, O. Bursi, F. Taucer, R. Ceravolo, P. Pegon, M. Poljansek, L. Zanotti Fragonara, M. Sartori, S. Alessandri, R. De Risi, and C. Yenidogan, "Assessment of the seismic vulnerability of an old RC viaduct with frame piers and study of the effectiveness of base isolation through PsD testing (RETRO).," tech. rep., Publications Office, Luxembourg, 2014.

[18] G. Abbiati, O. S. Bursi, P. Caperan, L. Di Sarno, F. J. Molina, F. Paolacci, and P. Pegon, "Hybrid simulation of a multi-span RC viaduct with plain bars and sliding bearings: Hybrid Simulations of a Multi-Span RC Viaduct," *Earthquake Engineering & Structural Dynamics*, vol. 44, no. 13, pp. 2221–2240, 2015.

[19] O. S. Bursi, G. Abbiati, E. Cazzador, P. Pegon, and F. J. Molina, "Nonlinear heterogeneous dynamic substructuring and partitioned FETI time integration for the development of low-discrepancy simulation models," *International Journal for Numerical Methods in Engineering*, vol. 112, no. 9, pp. 1253–1291, 2017.

[20] M. Dabaghi and A. D. Kiureghian, "Stochastic model for simulation of near-fault ground motions," *Earthquake Engineering & Structural Dynamics*, vol. 46, no. 6, pp. 963–984, 2017.

[21] G. Blatman and B. Sudret, "Adaptive sparse polynomial chaos expansion based on least angle regression," *Journal of Computational Physics*, vol. 230, no. 6, pp. 2345–2367, 2011.

[22] L. Le Gratiet, S. Marelli, and B. Sudret, *Metamodel-Based Sensitivity Analysis: Polynomial Chaos Expansions and Gaussian Processes*, pp. 1289–1325. Cham: Springer International Publishing, 2017.

[23] I. Abdallah, C. Lataniotis, and B. Sudret, "Parametric hierarchical kriging for multi-fidelity aero-servo-elastic simulators — Application to extreme loads on wind turbines," *Probabilistic Engineering Mechanics*, vol. 55, pp. 67–77, 2019.

[24] B. A. Bradley, "A generalized conditional intensity measure approach and holistic ground-motion selection," *Earthquake Engineering & Structural Dynamics*, pp. n/a–n/a, 2010.

[25] I. Iervolino, C. Galasso, and E. Cosenza, "REXEL: computer aided record selection for code-based seismic structural analysis," *Bulletin of Earthquake Engineering*, vol. 8, no. 2, pp. 339–362, 2010.

[26] J. W. Baker, "Conditional Mean Spectrum: Tool for Ground-Motion Selection," *Journal of Structural Engineering*, vol. 137, no. 3, pp. 322–331, 2011.

[27] T. Trucano, L. Swiler, T. Igusa, W. Oberkampf, and M. Pilch, "Calibration, validation, and sensitivity analysis: What's what," *Reliability Engineering & System Safety*, vol. 91, no. 10-11, pp. 1331–1357, 2006.

[28] R. R. Craig and A. J. Kurdila, *Fundamentals of structural dynamics.* John Wiley & Sons, 2006.

[29] Z.-H. Han and S. Görtz, "Hierarchical Kriging Model for Variable-Fidelity Surrogate Modeling," *AIAA Journal*, vol. 50, no. 9, pp. 1885–1896, 2012.

[30] A. Suzuki and I. Iervolino, "Intensity measure conversion of fragility curves," *Earthquake Engineering & Structural Dynamics*, vol. 49, no. 6, pp. 607–629, 2020.

[31] M. Grigoriu, "To Scale or Not to Scale Seismic Ground-Acceleration Records," *Journal of Engineering Mechanics*, vol. 137, no. 4, pp. 284–293, 2011.

[32] F. Pacor, R. Paolucci, L. Luzi, F. Sabetta, A. Spinelli, A. Gorini, M. Nicoletti, S. Marcucci, L. Filippi, and M. Dolce, "Overview of the Italian strong motion database ITACA 1.0," *Bulletin of Earthquake Engineering*, vol. 9, no. 6, pp. 1723–1739, 2011.

[33] F. McKenna, M. H. Scott, and G. L. Fenves, "Nonlinear Finite-Element Analysis Software Architecture Using Object Composition," *Journal of Computing in Civil Engineering*, vol. 24, no. 1, p. 13, 2010.

[34] F. Paolacci and R. Giannini, "An experimental and numerical investigation on the cyclic response of a portal frame pier belonging to an old reinforced concrete viaduct," *Earthquake Engineering & Structural Dynamics*, vol. 41, no. 6, pp. 1109–1127, 2012.

[35] F. Ikhouane and J. Rodellar, *Systems with hysteresis: analysis, identification and control using the Bouc-Wen model.* Chichester, England ; Hoboken, NJ: John Wiley, 2007.

[36] G. P. Mavroeidis, "A Mathematical Representation of Near-Fault Ground Motions," *Bulletin of the Seismological Society of America*, vol. 93, no. 3, pp. 1099–1131, 2003.

[37] P. Bazzurro and C. Allin Cornell, "Disaggregation of seismic hazard," *Bulletin of the Seismological Society of America*, vol. 89, no. 2, pp. 501–520, 1999.

[38] J. W. Baker, "Quantitative classification of near-fault ground motions using wavelet analysis," *Bulletin of the Seismological Society of America*, vol. 97, no. 5, pp. 1486–1501, 2007.

[39] M. Berveiller, B. Sudret, and M. Lemaire, "Stochastic finite element: a non intrusive approach by regression," *European Journal of Computational Mechanics*, vol. 15, no. 1-3, pp. 81–92, 2006.

[40] S. Alessandri, R. Giannini, and F. Paolacci, "Aftershock risk assessment and the decision to open traffic on bridges," *Earthquake Engineering & Structural Dynamics*, vol. 42, no. 15, pp. 2255–2275, 2013.

[41] R. De Risi, L. Di Sarno, and F. Paolacci, "Probabilistic seismic performance assessment of an existing RC bridge with portal-frame piers designed for gravity loads only," *Engineering Structures*, vol. 145, pp. 348–367, 2017.

[42] I. M. Sobol, "Sensitivity estimates for nonlinear mathematical models," *Mathematical modelling and computational experiments*, vol. 1, no. 4, pp. 407–414, 1993.

[43] A. Saltelli, M. Ratto, T. Andres, F. Campolongo, J. Cariboni, D. Gatelli, M. Saisana, and S. Tarantola, *Global Sensitivity Analysis. The Primer.* Chichester, UK: John Wiley & Sons, Ltd, 2007.

[44] B. Sudret, "Global sensitivity analysis using polynomial chaos expansions," *Reliability Engineering & System Safety*, vol. 93, no. 7, pp. 964–979, 2008.

[45] L. L. Gratiet, S. Marelli, and B. Sudret, "Metamodel-Based Sensitivity Analysis: Polynomial Chaos Expansions and Gaussian Processes," in *Handbook of Uncertainty Quantification* (R. Ghanem, D. Higdon, and H. Owhadi, eds.), pp. 1–37, Cham: Springer International Publishing, 2015.

[46] D. Xiu and G. E. Karniadakis, "The Wiener–Askey polynomial chaos for stochastic differential equations," *SIAM journal on scientific computing*, vol. 24, no. 2, p. 26, 2002.

[47] G. Deman, K. Konakli, B. Sudret, J. Kerrou, P. Perrochet, and H. Benabderrahmane, "Using sparse polynomial chaos expansions for the global sensitivity analysis of groundwater lifetime expectancy in a multi-layered hydrogeological model," *Reliability Engineering & System Safety*, vol. 147, pp. 156–169, 2016.

[48] D. Harenberg, S. Marelli, B. Sudret, and V. Winschel, "Uncertainty quantification and global sensitivity analysis for economic models," *Quantitative Economics*, vol. 10, no. 1, pp. 1–41, 2019.

[49] S. Marelli and B. Sudret, "UQLab: A Framework for Uncertainty Quantification in Matlab," in *Vulnerability, Uncertainty, and Risk*, (Liverpool, UK), pp. 2554–2563, American Society of Civil Engineers, 2014.

[50] S. Marelli and B. Sudret, "UQLab user manual – Polynomial chaos expansions," tech. rep., Chair of Risk, Safety and Uncertainty Quantification, ETH Zurich, Switzerland, 2019.

[51] S. Marelli, C. Lamas, K. Konakli, C. Mylonas, P. Wiederkehr, and B. Sudret, "UQLab user manual – Sensitivity analysis," tech. rep., Chair of Risk, Safety and Uncertainty Quantification, ETH Zurich, Switzerland, 2019.

[52] C. E. Rasmussen and C. K. I. Williams, *Gaussian processes in machine learning.* Cambridge, Massachusetts: MIT Press, 2006.

[53] N. Cressie, *Statistics for spatial data*, vol. 4. Wiley Online Library, 1992.

[54] T. Santner, B. Williams, and W. Notz, *The design and analysis of computer experiments.* New York, NY: Springer, 2003.

[55] V. Dubourg, *Adaptive surrogate models for reliability analysis and reliability-based design optimization.* PhD thesis, Universite' Blaise Pascal, Clermont-Ferrand II, 2011.

[56] C. Lataniotis, D. Wicaksono, S. Marelli, and B. Sudret, "UQLab user manual – Kriging (Gaussian process modeling)," tech. rep., Chair of Risk, Safety and Uncertainty Quantification, ETH Zurich, Switzerland, 2019.